FRONTIERS OF PHYSICS

REVIEW ARTICLE
Volume 21 / Issue 11 / 114301 / 2026

MXenes for advanced energy storage: A computational perspective

Hejing Wang (王鹤静)[1], Beibei Shi (石蓓蓓)[1], Yixiao Zhang (张一笑)[1], Yongzheng Fang (方永正)[1], Xu Zhang (张旭)[1,2,†], Menggai Jiao (焦梦改)[1,2,‡], Zhen Zhou (周震)[1,2]

1 Interdisciplinary Research Center for Sustainable Energy Science and Engineering (IRC4SE[2]), School of Chemical Engineering, Zhengzhou University, Zhengzhou 450001, China
2 National Key Laboratory of Special Rare Metal Materials, Zhengzhou University, Zhengzhou 450001, China
Corresponding authors. E-mail: †zzuzhangxu@zzu.edu.cn, ‡mgjiao@zzu.edu.cn
Received December 6, 2025; accepted February 13, 2026

ABSTRACT

The urgent demand for sustainable energy solutions has accelerated the development of rechargeable batteries, where the design of high-performance electrode materials plays a pivotal role. Since their discovery in 2011, two-dimensional (2D) transition metal carbides and nitrides, known as MXenes, have garnered significant attention owing to their excellent electrical conductivity, high mechanical strength, tailorable surface chemistry, and large specific surface area with abundant active sites. These unique properties render MXenes highly promising for electrochemical energy storage, particularly in lithium–ion, lithium–sulfur, and lithium–oxygen batteries, as well as emerging non-lithium–ion battery systems. However, their practical implementation is hindered by critical challenges including structural restacking, poor stability, and unfavorable surface terminations. In this review, we focus on a computational perspective for the rational design and performance optimization of MXene-based electrodes. Density functional theory (DFT) calculations have yielded fundamental insights into the intrinsic properties, modification mechanisms, and electrochemical behaviors of MXenes. Additionally, machine learning has enabled high-throughput screening and predictive modeling of their structure–property relationships. More importantly, this review not only summarizes the theoretical advances in MXenes for energy storage applications but also extracts actionable theoretical insights and performance prediction principles. These efforts provide a comprehensive theoretical reference for computational studies on MXenes, allowing researchers to efficiently grasp the research landscape, core mechanisms, and modification strategies. Furthermore, this review offers targeted guidance for experimental investigations by facilitating the optimization of modification schemes, the selection of suitable battery systems, and the reduction of trial-and-error in experimental design.

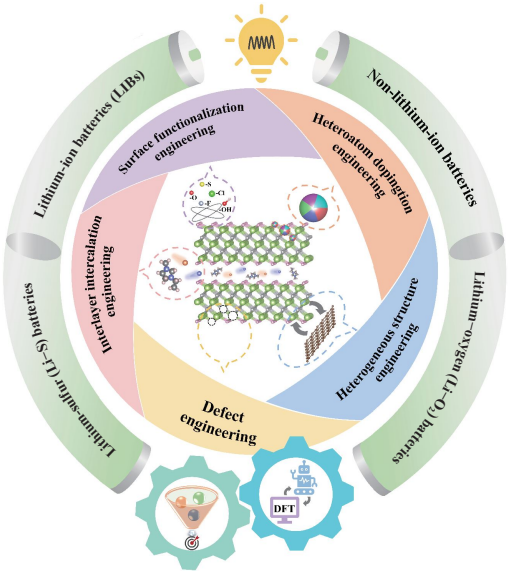

Keywords MXenes, energy storage, density functional theory, machine learning, rechargeable batteries

*Special Topic: Celebrating the 20th Anniversary of the Founding of Frontiers of Physics (Editors: Zhimin Liao, Jun He & Huabing Yang).

Higher Education Press

https://doi.org/10.15302/frontphys.2026.114301

Contents

1 Introduction

Environmental pollution and ecological challenges posed by conventional fossil fuels have necessitated a strategic transition of energy infrastructure toward renewable sources, which is recognized as an inevitable trend for sustainable development in contemporary society [1–3]. Consequently, the efficient utilization of green energy imposes greater demands on energy storage and conversion technologies [4]. Owing to the relatively high energy density and cycling efficiency, rechargeable batteries demonstrate significant potential in the field of electrochemical energy storage, encompassing lithium-ion batteries (LIBs), lithium–sulfur (Li–S) batteries, lithium–oxygen (Li–O_2) batteries, as well as non-lithium-ion battery systems [5–7]. The rapid development of commercial applications such as portable electronic devices, new-energy vehicles, and smart grid systems has intensified the demand for rechargeable batteries with higher energy density, improved cycling stability, and enhanced safety. Consequently, the design and development of high-performance electrode materials have emerged as a critical focus for advancing current research in electrochemical energy storage.

Since the first synthesis of Ti_3C_2 in 2011 [8], two-dimensional (2D) transition metal carbides and nitrides (defined as MXenes) have garnered widespread research attention due to their distinctive combination of properties, including excellent metallic conductivity, remarkable mechanical performance, and a high specific surface area with abundant active sites [9]. MXenes possess the general chemical formula $M_{n+1}X_nT_x$ (n = 1–4, $x \leq 2$), where M represents an early transition metal [green elements in Fig. 1(a)], X denotes C and/or N, and, more recently, O [10, 11] [gray elements in Fig. 1(a)], while T signifies surface termination groups [marked in orange in Fig. 1(a)]. The synthesis process of MXenes is illustrated in Fig. 1(b). MXenes are derived from MAX phase precursors [where A represents an A-group element, red-labeled in Fig. 1(a)], characterized by alternating MX layers and A atomic layers. In MAX phases, M–A bonds (metallic bonding) are weaker than M–X bonds (covalent/ionic bonding), while A-layer elements exhibit higher reactivity than the $M_{n+1}X_n$ framework. Consequently, the A layers can be selectively removed from MAX precursors through chemical etching, yielding multilayer MXenes [12, 13]. Subsequent exfoliation allows these multilayer MXenes to be delaminated into single- to few-layer sheets. During this process, dangling bonds are generated on the M-layer surface and are rapidly saturated through reactions with environmental termination groups (T_x) [14]. It has been demonstrated that regulating the surface termination groups can chemically modify MXenes, thereby endowing them with diverse physicochemical properties to meet the demands of various applications.

Benefiting from the aforementioned advantages, MXenes have demonstrated broad application potential in cutting-edge fields such as electrochemical energy storage [15–17], sensing [18], catalysis [19–21], and biomedicine [22, 23], as evidenced by the remarkable surge in MXene-related publications [Fig. 1(c)]. Among these applications, energy storage accounts for a substantial proportion, particularly in rechargeable batteries, with the number of publications on MXenes in battery applications steadily increasing (based on the keywords “MXene” and “batter*” in the Web of Science database). Meanwhile, the network visualization map [Fig. 1(d)] highlights MXene materials as a major research hotspot among numerous keywords in battery research [24]. With the continuous discovery of new MXenes, these materials are expected to serve as promising candidates for advancing energy storage technologies. However, their practical applications still face serious challenges that need to be addressed, including instability, low capacity, interlayer restacking during charge-discharge cycles, and undesirable surface functional groups [25–27]. To enhance their performance as electrode materials, extensive efforts have been devoted to developing targeted modification strategies [28–32]: (i) Surface functionalization engineering, (ii) Heteroatom doping engineering, (iii) Defect engineering, (iv) Interlayer interca-

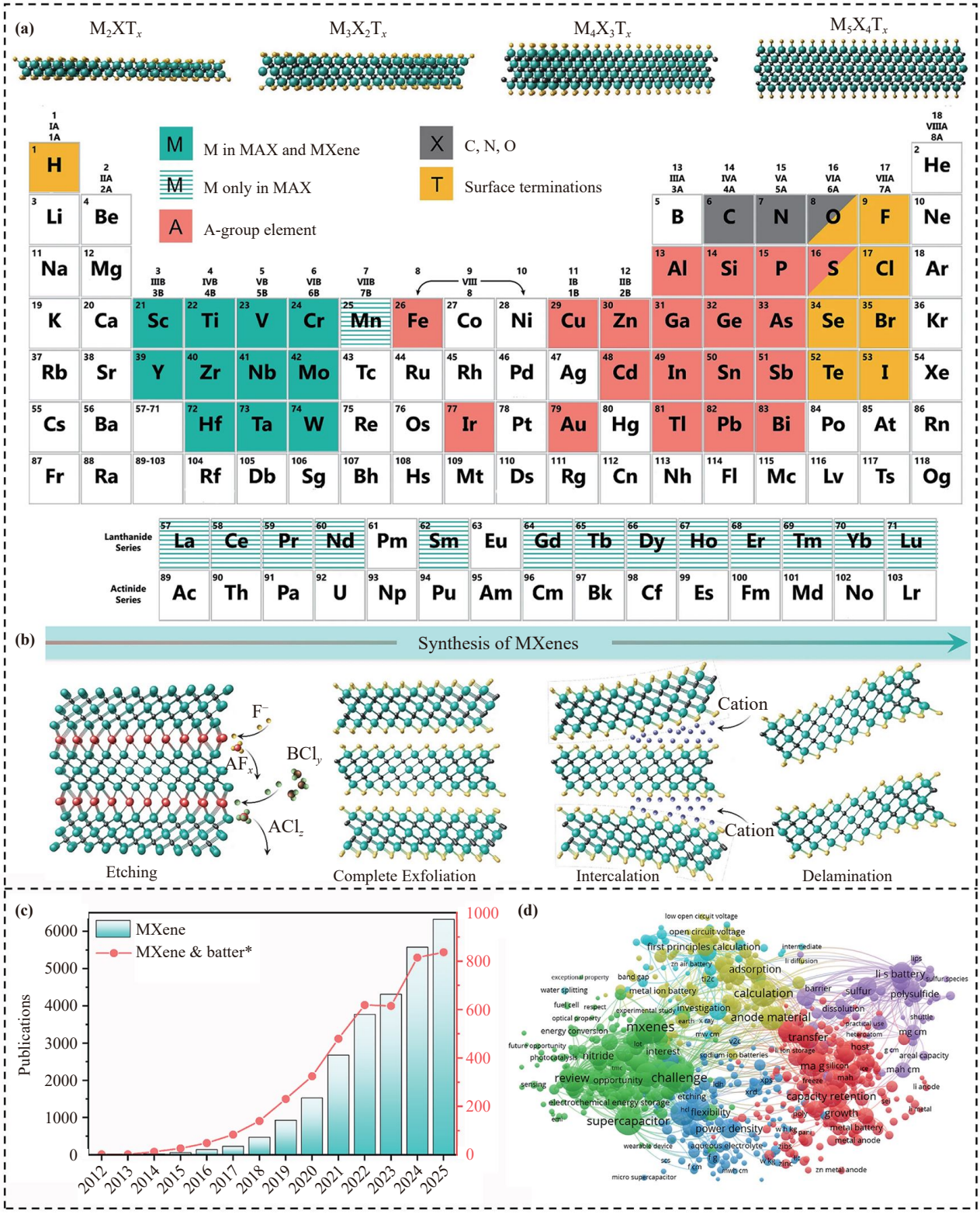

Fig. 1 **(a)** Crystal structure of MXenes and the distribution of their constituent elements in the periodic table. **(b)** Synthesis process of MXenes. The precursor MAX phase is etched to remove the A-layer elements, resulting in weakly bonded MXene multilayers, which are then separated into single-layer MXenes through cation intercalation. Reproduced with permission from Ref. [11]. Copyright © 2023 Springer Nature. **(c)** Publications from 2012 to 2025 were analyzed with "MXene", "MXene and batter*" as topics, based on data from the Web of Science. **(d)** Network visualization of MXene and applications in recent years. Reproduced with permission from Ref. [24]. Copyright © 2024 American Chemical Society.

lation engineering, and (v) Heterogeneous structure engineering.

It is widely recognized that battery performance arises from the complex interplay among multiple components. However, conventional experimental optimization is often time-consuming, repetitive, and costly, which limits the ability to tailor MXene properties for specific applications. Density functional theory (DFT) calculations offer a powerful alternative, providing valuable insights into the physicochemical properties, adsorption behaviors, and modification mechanisms of MXenes, all of which are closely correlated with their electrochemical performance. Furthermore, combining DFT with machine learning (ML) enables both high-throughput screening and the efficient prediction of MXenes with desired electrochemical properties by revealing their underlying design principles.

While numerous reviews have been published on the progress and challenges of MXenes in battery applications, most have primarily focused on experimental findings [24, 33]. In contrast, this review presents a comprehensive overview from a computational perspective, systematically summarizing recent advances in MXenes as electrode materials, and further providing actionable design guidance through the establishment of structure-property-performance relationships derived from DFT and ML studies. The discussion emphasizes the rational structure design, detailed analysis of structural characteristics, and exploration of energy storage mechanisms and performance. Specifically, this review outlines modification strategies to enhance MXene electrodes, examines their applications in LIBs, Li–S, Li–O_2, and non-lithium-ion batteries, and highlights the role of ML in guiding MXene research. Finally, future prospects and challenges for MXenes as electrode materials are summarized to inspire further exploration of high-performance electrochemical energy-storage systems.

2 Strategies to enhance the performance of MXene-based electrode materials

Over the past decade, MXenes have garnered significant research interest and experienced rapid development, demonstrating considerable potential in rechargeable battery applications. Nonetheless, the intrinsic limitations of pristine MXenes as electrode materials severely hinder their practical implementation in high-performance systems [34–36]. Analogous to other 2D materials, the high surface chemical reactivity of MXenes makes them prone to restacking, which poses a significant challenge for energy storage applications. Notably, the interlayer interactions in MXenes involve not only van der Waals forces but also hydrogen-bonding networks formed between neighboring –OH and –O/–F terminations. The synergistic effects of these interactions drive the restacking of MXene sheets, which markedly decreases the accessible surface area, impedes ion transport kinetics, and induces severe volume variations. In addition, MXenes are highly susceptible to oxidation under aqueous environments, potentially triggering structural collapse and performance degradation, while unfavorable surface terminations further restrict their capacity [37, 38]. Overall, developing effective modification strategies is of paramount importance for improving the electrochemical performance of MXene materials [39].

2.1 Surface functionalization engineering

As investigations into MXenes have deepened, it has been found that the surface functional groups of MXenes, prepared through distinct etching methods and post-treatment processes, differ significantly. These variations can markedly affect their hydrophilicity, electronic structure, and electrochemical behavior. To date, a variety of approaches have been employed to modify the surface of MXenes, resulting in a wide spectrum of terminations, including –OH, –NH, –F, –Cl, –Br, –O, –S, –Se, –Te, and –SO_3H [40, 41]. These differences in surface terminations directly modulate the charge storage characteristics of MXenes. Even when governed by the same intercalation mechanism, materials may exhibit different theoretical specific capacities. For example, MXenes synthesized via the conventional HF solution etching method typically contain abundant –F, –O, and –OH functional groups [42, 43]. Among them, the –F and –OH terminations are electrochemically inert, contributing little to the overall capacity while potentially impeding ion transport and suppressing redox reactions, thereby reducing electrochemical efficiency. In contrast, O functionalized surfaces can enhance the hydrophilicity of MXenes, facilitating more efficient ion transport and storage [44]. Typically, three possible termination configurations can be identified when theoretically investigating surface functional groups, as presented in Fig. 2(a) (taking the –F termination as an example) [45]. According to theoretical research summarized by Tang *et al.* [45] and Xie *et al.* [46], the specific capacities of bare Ti_3C_2 and MXenes terminated with –O, –F, and –OH groups are 320, 268, 130, and 67 $mA{\cdot}h{\cdot}g^{-1}$, respectively [Fig. 2(b)]. Moreover, the Li^+ diffusion ability follows the order of Ti_3C_2 > $Ti_3C_2O_2$ > $Ti_3C_2F_2$ > $Ti_3C_2(OH)_2$. These results indicate that –O terminations deliver the highest double-layer lithium storage capacity among the three functionalized Ti_3C_2 variants, while –F and –OH groups suppress Li^+ adsorption and hinder diffusion kinetics. Consequently, the experimentally observed capacity of Ti_3C_2 is often only about half of its theoretical value. This pronounced discrepancy can mainly be attributed to idealized theoretical models that assume a termination-free Ti_3C_2 structure, while in practice the formation of –F and –OH terminations during synthesis

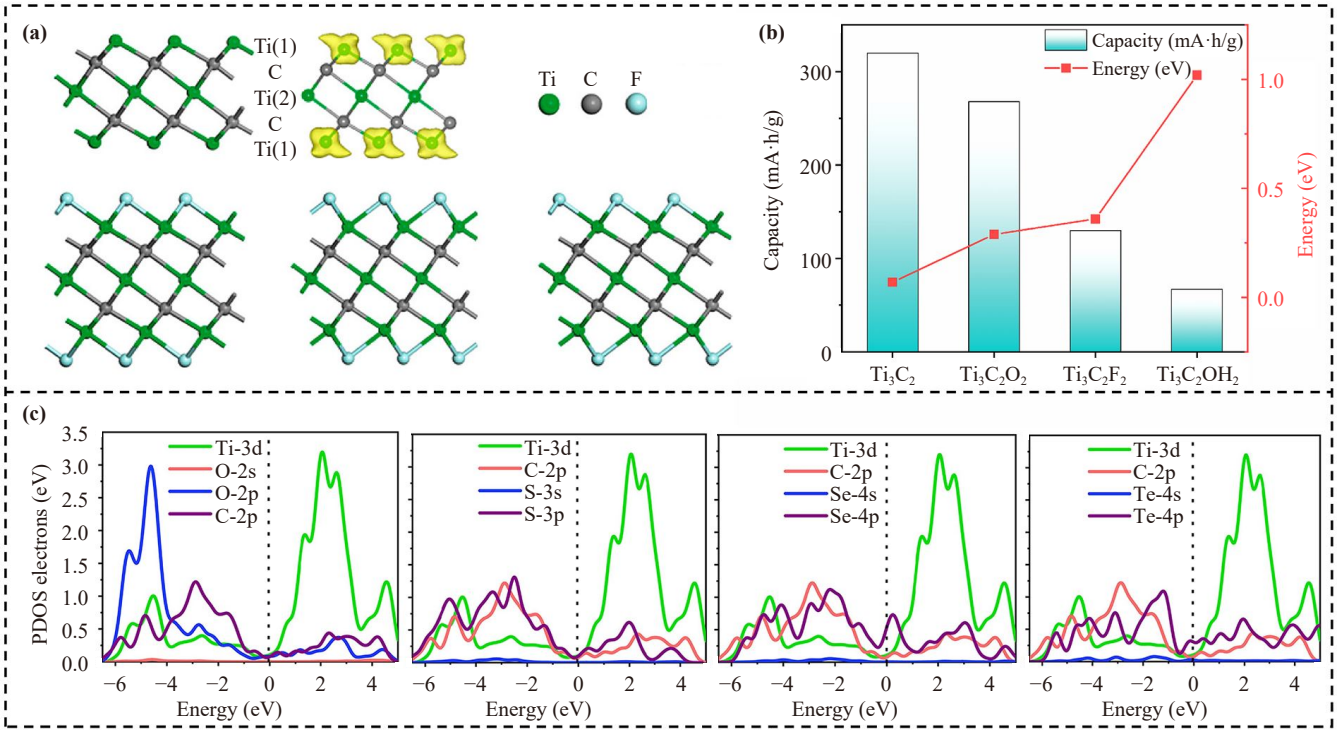

Fig. 2 **(a)** Side view of pristine Ti_3C_2 and three possible configurations for $Ti_3C_2F_2$. Reproduced with permission from Ref. [45]. Copyright © 2012 American Chemical Society. **(b)** Theoretical storage capacities and Li^+ migration energy barriers of bare Ti_3C_2 and $Ti_3C_2T_2$ (T = F, O, and OH). **(c)** Calculated PDOS of the $Ti_3C_2T_2$ (T = O, S, Se, and Te). Reproduced with permission from Ref. [52]. Copyright © 2020 Elsevier.

is unavoidable and severely limits the achievable capacity [47]. To mitigate the detrimental effects of unfavorable surface terminations (–OH and –F), inexpensive alkaline reagents such as LiOH, KOH, $Mg(OH)_2$, and NaOH are often employed for the post-treatment of MXenes [48]. This strategy enables the replacement of –F terminations with –OH groups and charge-compensating cations (e.g., –Li, –K, –Mg, and –Na). Subsequent annealing can further convert –OH groups into –O terminations, resulting in MXene surfaces predominantly decorated with –O and cationic species. This surface reconstruction not only enhances the mechanical robustness of MXenes but also significantly improves their electrochemical performance, in good agreement with theoretical predictions.

In addition, the electrical conductivity of MXenes is closely associated with their surface terminations. The transfer of electrons from the transition metal layers to the negatively charged terminations induces charge redistribution and alters transport characteristics, thereby regulating the overall conductivity of MXene [49]. Moreover, the incorporation of surface functional groups causes a downward shift of the Fermi level, which consequently diminishes the electrical conductivity compared with pristine MXenes [50, 51]. Li *et al.* [52] investigated the electronic properties of chalcogenized-Ti_3C_2 ($Ti_3C_2T_2$, T = O, S, Se, and Te) MXenes. Notably, the calculated partial density of states (PDOS), as illustrated in Fig. 2(c), reveals that chalcogenation disrupts the intrinsic magnetism of pristine Ti_3C_2, resulting in a non-magnetic ground state. However, this modification does not alter the metallic nature of Ti_3C_2, as evidenced by the pronounced electronic states located near Fermi level. Such metallic behavior enables a high density of charge carriers, endowing these materials with promising potential as electrode candidates for ion batteries.

2.2 Heteroatom doping engineering

Inspired by the diverse doping strategies employed in graphene, heteroatom doping has been proven to be an effective approach for optimizing the properties of pristine MXenes. By introducing local lattice distortions and modulating the atomic coordination environment, this strategy enables structural tailoring at the atomic scale, thereby refining the electronic structure and enhancing charge transport characteristics. As a result, synergistic improvements in electrical conductivity, ion transport kinetics, and overall electrochemical performance can be achieved. Heteroatom doping, encompassing both nonmetallic and metallic dopants, typically occurs at

three sites within MXenes: the M, X, and T sites. Owing to the compositional diversity and stoichiometric flexibility inherent in MXene structures, such doping modifications offer precise control over their physicochemical properties.

2.2.1 Metallic element doping

Metal element doping in MXenes generally refers to the substitution of transition metals (e.g., Mo, V, Cr) at the M sites. Since MXenes inherently contain transition metals, introducing additional transition metal dopants is considered one of the most effective strategies to enhance their properties. It is widely recognized that the unique properties of MXenes primarily originate from the partially occupied d orbitals of transition metals. These d orbitals not only govern the electronic structure and the density of states near Fermi level, but also play a crucial role in determining the electrical conductivity and transport characteristics of the material [53–55]. For instance, computational studies by Khazaei *et al.* [56] reveal that, within the same group of transition metals (Ti, Zr, and Hf), the band gap of the corresponding MXenes increases with the atomic number, exhibiting the trend $Hf_2CO_2 > Zr_2CO_2 > Ti_2CO_2$ [Fig. 3(a)]. In 2019, Kuznetsov *et al.* [57] introduced Co into Mo_2CT_x [Fig. 3(b)], with extended X-ray absorption fine structure (EXAFS) analysis confirming that the Co atoms occupy Mo lattice positions. This arrangement provides isolated Co centers without any detectable formation of other cobalt-containing phases, thereby successfully extending MXenes toward mid-to-late transition metal systems and further expanding the compositional space of the MXene family. Recently, Li *et al.* [58] conducted a systematic investigation into the effect of transition-metal doping Ti_2CO_2 (TM-Ti_2CO_2) on the lithium storage properties. The incorporation of eight distinct dopants (Sc, V, Cr, Mn, Fe, Co, Ni, and Cu) induces variations in the d-band center, which, as illustrated in Fig. 3(c), exhibit an approximately linear relationship with the Li adsorption energy (E_{ads}). In contrast to the pristine Ti_2CO_2, doping with Sc, Cr, and Mn atoms leads to an increase in the migration energy barrier, whereas the incorporation of V atoms effectively reduces the barrier to 0.11 eV [Fig. 3(d)]. Combined with a suitable open-circuit voltage (OCV, typically within 0–1.0 V for metal-ion batteries, where lower values are typically associated with higher output voltage and improved energy density), V-Ti_2CO_2 exhibits outstanding comprehensive performance, featuring an OCV of 0.66 V and a high theoretical capacity of 765.3 $mA{\cdot}h{\cdot}g^{-1}$. More recently, high-entropy MXenes (HE-MXenes) have emerged as a new class of 2D materials, attracting increasing attention owing to their multi-component tunability and the unique physicochemical properties derived from high-entropy effects. The first HE-MXene, $(Ti_{1/5}V_{1/5}Zr_{1/5}Nb_{1/5}Ta_{1/5})_2C$, was introduced by Du *et al.* [59] in 2021. This HE-MXene is synthesized by selectively etching a novel HE-MAX phase, $(Ti_{1/5}V_{1/5}Zr_{1/5}Nb_{1/5}Ta_{1/5})_2AlC$ [Fig. 3(e)], in which five size-compatible and infusible transition metal elements render the MXene atomic layers highly stable. Moreover, the resultant HE-MXene atomic layers exhibit pronounced lattice distortions, inducing significant mechanical strain. Such strain effectively regulates the nucleation and uniform growth of dendrite-free lithium on HE-MXene, enabling stable cycling performance for up to 1200 h, as illustrated in Figs. 3(f) and (g). This breakthrough confirms the outstanding electrochemical properties of HE-MXene and provides valuable guidance for their rational design and optimization toward energy storage applications.

2.2.2 Non-metallic element doping

According to prior studies, heteroatoms such as N, O, S, or P can be doped at all three sites (M, X, T), whereas halogens are typically substituted at T sites [60]. Among the various non-metallic dopants, nitrogen is one of the most extensively employed elements due to its pronounced effect on enhancing material performance. In the case of M_3C_2 MXenes, substitution of 50% of the carbon sites with nitrogen atoms results in the formation of hetero-N-MXenes (transition metal carbonitrides, M_3CN). Owing to the higher electronegativity of nitrogen, the resulting M–N bonds are stronger than M–C bonds, endowing the material with superior physical and electronic properties compared with pristine M_3C_2 MXenes. Zhang *et al.* [61] systematically investigated the electrochemical behavior of Ti_3CNO_2, $Ti_3C_2O_2$, and $Ti_3N_2O_2$ [Fig. 4(a)] as anode materials for sodium-ion batteries (SIBs). It was found that the O–Ti–N interaction is stronger than the O–Ti–C interaction, resulting in tighter stacking in Ti_3CNO_2 and $Ti_3N_2O_2$, along with a larger interlayer spacing compared with $Ti_3C_2O_2$, which is favorable for the sodiation/desodiation process. As illustrated in Fig. 4(b), relatively low diffusion energy barriers were observed for Ti_3CNO_2 and $Ti_3N_2O_2$, with values of 0.123 and 0.04 eV, respectively, corroborated by the experimentally measured rate performance. Notably, Fig. 4(c) shows that Ti_3CNT_x exhibits superior cycling stability compared with $Ti_3C_2T_x$ after 200 cycles, underscoring its promise as a high-performance anode material for sodium-ion batteries. Furthermore, Lu *et al.* [62] conducted a comprehensive investigation into the potential mechanisms of N doping, focusing particularly on the positions of the dopants and their influence on the electronic properties of MXenes. Through comparison of the formation energies of all possible N arrangements in $Ti_3C_2T_x$ (T = O, F, and OH), three energetically most favorable doping configurations were identified: lattice substitution of C atoms (LS), substitution of –OH functional groups (FS), and surface adsorption at

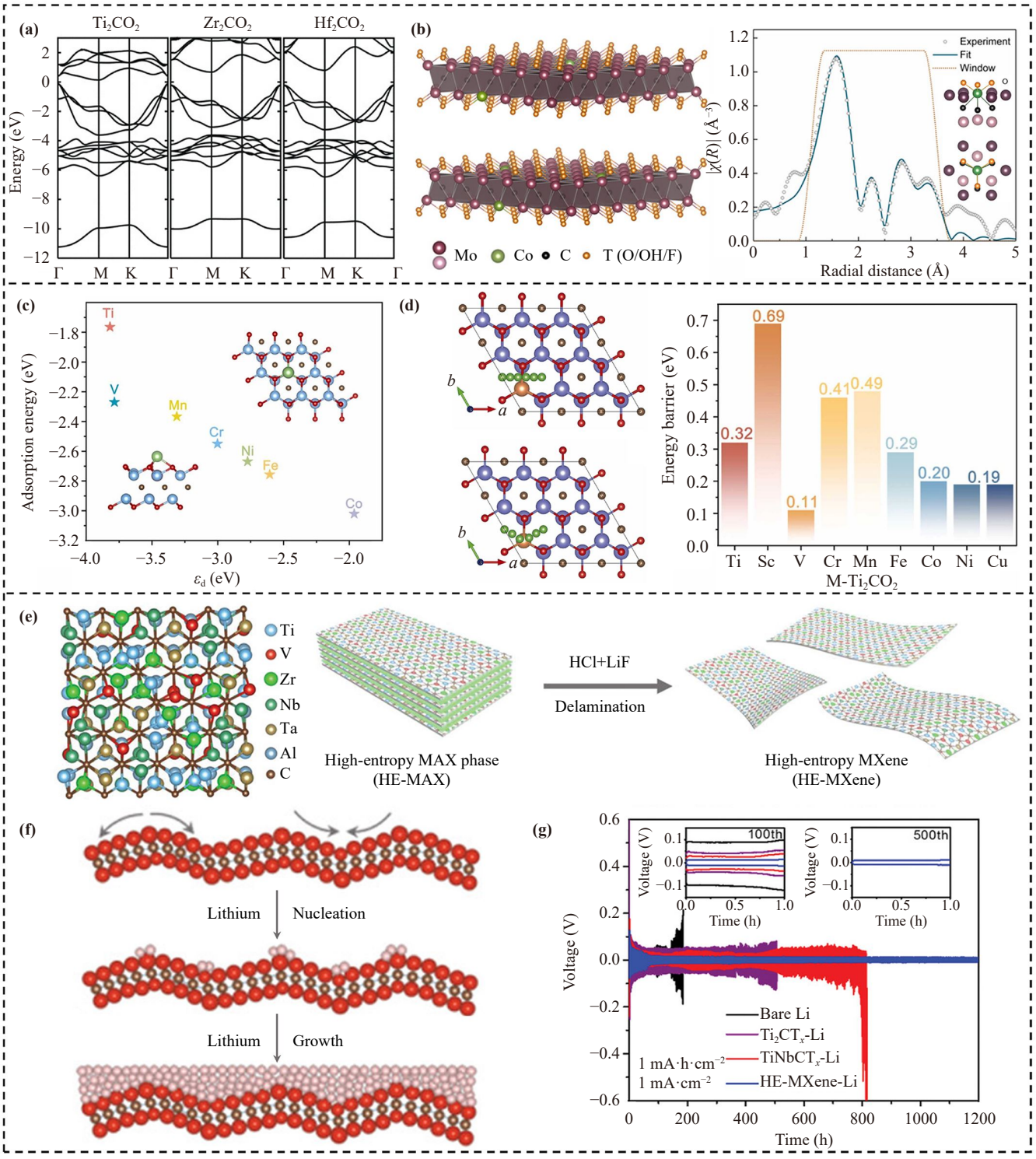

Fig. 3 **(a)** Electronic band structures of Hf_2CO_2, Zr_2CO_2, and Ti_2CO_2 MXene. Reproduced with permission from Ref. [56]. Copyright © 2012 John Wiley and Sons. **(b)** Structural characterization of Co-Mo_2CT_x by EXAFS, together with a schematic diagram of the Co coordination environment. Reproduced with permission from Ref. [57]. Copyright © 2019 American Chemical Society. **(c)** The relationship between the E_{ads} of Li on different doped metals and the d-band center. **(d)** The diffusion paths and energy barriers of Li on different TM-Ti_2CO_2 monolayers. Reproduced with permission from Ref. [58]. Copyright © 2024 Elsevier. **(e)** Crystal structure of the $(Ti_{1/5}V_{1/5}Zr_{1/5}Nb_{1/5}Ta_{1/5})_2AlC$ HE-MAX phase and schematic illustration of HE-MXene synthesis from HE-MAX through a hydrogen chloride/lithium fluoride etching process. **(f)** Schematic illustration of strain-guided lithium nucleation and growth on HE-MXene atomic layers. **(g)** Cycling stability of symmetric cells based on HE-MXene-Li in comparison with TiNbT_x-Li, Ti_2CT_x-Li, and bare Li. Reproduced with permission from Ref. [59]. Copyright © 2021 John Wiley and Sons.

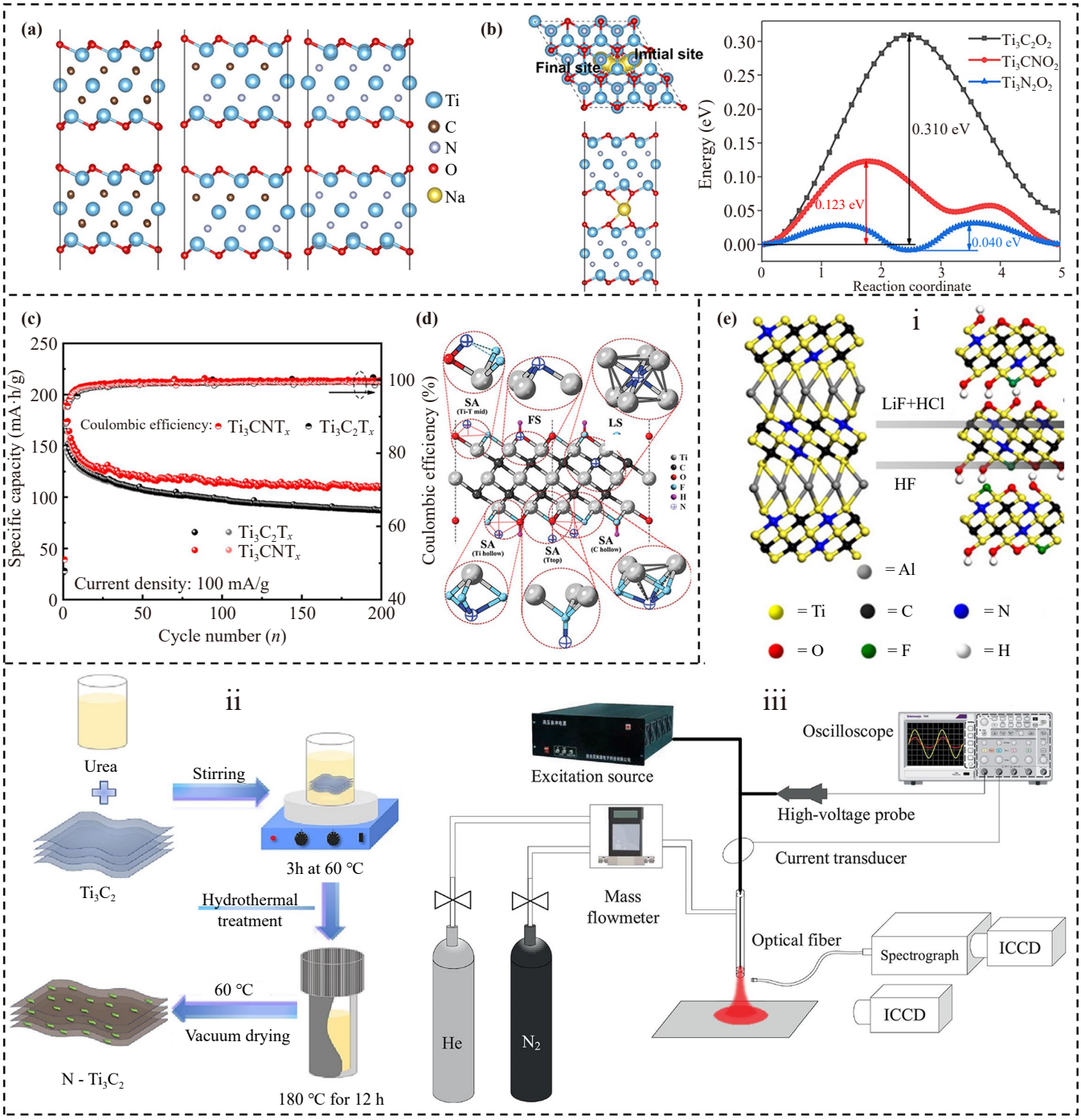

Fig. 4 **(a)** Structure models of $Ti_3C_2O_2$, Ti_3CNO_2, and $Ti_3N_2O_2$ MXene. **(b)** Diffusion paths and energy barriers of Na intercalated into $Ti_3C_2O_2$, Ti_3CNO_2, and $Ti_3N_2O_2$. **(c)** Cycle stability of $Ti_3C_2T_x$ and Ti_3CNT_x at a current density of 100 mA/g. Reproduced with permission from Ref. [61]. Copyright © 2021 American Chemical Society. **(d)** Schematic illustration of all possible nitrogen doping sites in $Ti_3C_2T_x$. Reproduced with permission from Ref. [62]. Copyright © 2020 John Wiley and Sons. **(e)** Three N-doping strategies: (i) in situ etching from Ti_3AlCN. Reproduced with permission from Ref. [63]. Copyright © 2019 American Chemical Society), (ii) hydrothermal treatment. Reproduced with permission from Ref. [60]. Copyright © 2023 Elsevier, and (iii) cold plasma technique. Reproduced with permission from Ref. [64]. Copyright © 2024 John Wiley and Sons.

–O terminations (SA) [Fig. 4(d)]. These configurations were respectively realized using the following synthesis strategies [Fig. 4(e)]: (i) in situ etching of the MAX phase Ti_3AlCN [63], (ii) hydrothermal treatment of

Ti_3C_2 MXene with urea [60], and (iii) cold plasma treatment of Ti_3C_2 MXene under pure N_2 [64]. Each doping mechanism exerts a distinct influence on the structural stability and electrochemical properties of MXenes. Motivated by the promising features of N-doping reported earlier, Ahmed *et al.* [65] further explored the regulatory effect of nitrogen concentration on Ti_2C. The calculation results revealed that with increasing nitrogen concentration, a significant enhancement in the density of states near Fermi level is observed. This enhancement signifies an increase in carrier concentration and electron mobility, which consequently improves electrical conductivity and modifies electronic transport behavior.

2.3 Defect engineering

In 2D materials, intrinsic defects are almost inevitable during experimental synthesis. Generally, intrinsic defects in MXenes can be categorized into vacancy defects and active edge defects [66]. Vacancy defects originate from the absence of certain atoms in the MXene lattice, primarily including vacancies at the X site and M site vacancies, while active edge defects are associated with the boundaries or pore structures of the nanosheets. The presence of these defects alters the surrounding atomic arrangement and coordination environment, endowing the materials with novel physical properties and functionalities. Carbon vacancies, commonly observed in MAX phases, are frequently inherited by the corresponding MXene derivatives. Hu *et al.* [67] employed first-principles calculations to explore the effects of introducing carbon vacancies on the structure and physicochemical properties of Ti_2CT_2, with the model of carbon-vacant (labeled as V_C) Ti_2CO_2 presented in Fig. 5(a). In contrast to other prototypical 2D materials such as graphene and MoS_2, Ti_2CT_2 exhibits a relatively low vacancy formation energy, implying a tendency for defect generation [Fig. 5(b)]. Subsequent lattice dynamics analysis combined with ab initio molecular dynamics (AIMD) simulations confirmed that V_C-Ti_2CO_2 remains both thermodynamically and dynamically stable. More importantly, the introduction of carbon vacancies enhances the electronic conductivity and flexibility of Ti_2CT_2, which benefits its performance in energy storage devices. Wu *et al.* [68] systematically investigated the formation of single M vacancies (defined as V_M) in M_2C MXenes (M = Sc, Ti, V, Zr, Nb, Mo, Hf, Ta, and W) and their effects on Li adsorption and diffusion. Their results indicate that, among all the examined M_2C systems, Mo_2C is the most favorable for V_M formation, exhibiting the lowest vacancy formation energy of 0.96 eV [Fig. 5(c)]. Although the relatively high diffusion barriers of 0.93–0.94 eV hinder Li escape from V_M sites and may negatively affect Li deintercalation, Li diffusion preferentially occurs at the flat surface, with much lower isotropic barriers of 0.096–0.115 eV. In contrast, migration into vacancy sites requires overcoming significantly higher barriers of 0.258–0.321 eV [Fig. 5(d)]. Overall, the vacancy-induced potential trap has a limited effect on Li diffusion and thus exerts minimal influence on the rate capability of LIBs. Moreover, the presence of V_M reduces the effective molecular weight of the host lattice, resulting in an enhanced theoretical capacity of 542 $mA{\cdot}h{\cdot}g^{-1}$ compared with 526 $mA{\cdot}h{\cdot}g^{-1}$ for pristine Mo_2C.

Although defects can increase the surface activity of MXenes, they simultaneously make the materials more prone to oxidation and corrosion in electrolytes. In particular, excessive defects may compromise their oxidation stability, which necessitates effective suppression and mitigation strategies. By tuning the concentration of the etchant (HF produced from the reaction of LiF and HCl) during synthesis, Li *et al.* [69] successfully achieved controllable preparation of Ti vacancies in MXenes [Fig. 5(e)]. An increase in the Ti vacancy count was observed with higher HF concentrations, which aligns well with the statistical analysis [Fig. 5(f)]. Furthermore, Ibragimova *et al.* [70] systematically investigated the effects of mixed surface terminations and chemical environments (pH and electrode potential) on defect formation. The results indicated that Ti vacancies are more stable on bare or OH-terminated surfaces, while C and N vacancies preferentially form on O-terminated surfaces. The computational scheme employs chemical potentials derived from Pourbaix diagrams [Fig. 5(g)] to construct formation energy maps [Fig. 5(h)] that are explicitly dependent on electrode potential and pH. These findings enable the prediction of conditions that favor extensive vacancy formation, offering valuable guidance for future experimental efforts: not only in suppressing excessive defect generation but also in forecasting synthesis parameters for achieving desired defect concentrations.

2.4 Interlayer intercalation engineering

In layered MXenes, the interlayer spacing exerts a significant influence on their electrochemical performance. By introducing appropriate intercalation species, such as organic molecules and ions, into multilayer MXenes, targeted modulation of their properties can be achieved to meet diverse application demands. These intercalants not only establish a supporting framework that prevents restacking and enlarges the interlayer spacing, thereby improving cycling stability, but also weaken the interlayer interactions, which promotes faster ion diffusion kinetics and ultimately enhances electrochemical performance.

Metal cation intercalation is a vital strategy for regulating the interlayer environment of MXenes at the atomic scale. Among various intercalants, metal cations possess unique advantages due to their charge and inher-

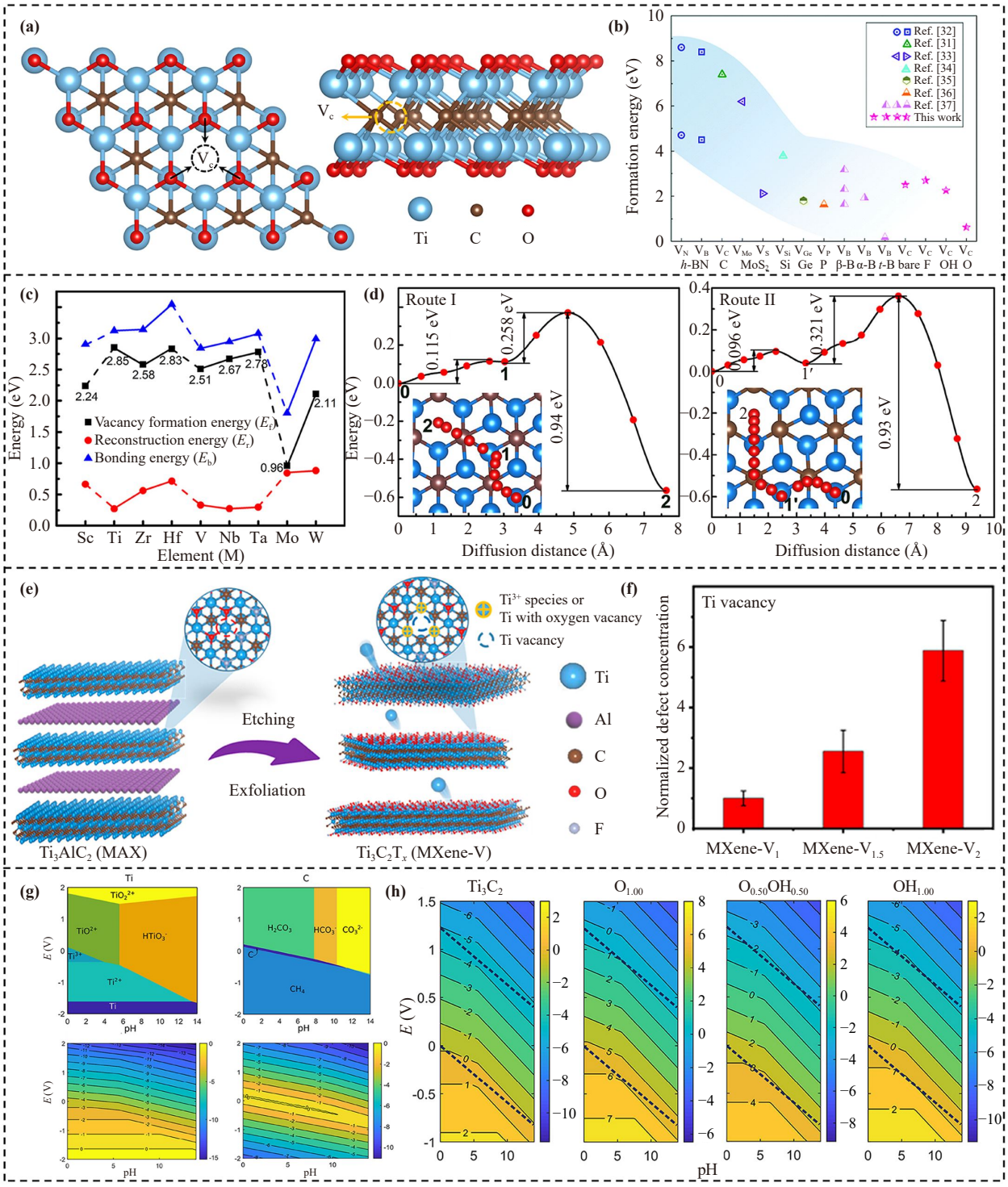

Fig. 5 **(a)** Local atomic structures of carbon-vacant Ti_2CO_2 MXene. **(b)** Vacancy formation energies of Ti_2CT_2 (T = O, F, and OH) compared with representative 2D materials. Reproduced with permission from Ref. [67]. Copyright © 2017 Royal Society of Chemistry. **(c)** Formation energy of a M vacancy on various M_2C. **(d)** The energy barrier of Li atom under two diffusion paths on defect Mo_2C. Reproduced with permission from Ref. [68]. Copyright © 2019 Elsevier. **(e)** Schematic illustration of the synthesis of MXene nanosheets with Ti lattice vacancies. **(f)** Normalized Ti vacancy concentrations derived from atomic-resolution HAADF-STEM analysis. Error bars denote the standard deviation for different MXene with Ti vacancy samples. Reproduced with permission from Ref. [69]. Copyright © 2025 American Chemical Society. **(g)** Pourbaix diagram of Ti and C in solution and the corresponding chemical potentials. **(h)** Formation energy of the Ti vacancy as a function of pH and electrode potential for bare Ti_3C_2 and $Ti_3C_2T_x$. Reproduced with permission from Ref. [70]. Copyright © 2022 American Chemical Society.

ently small size, enabling precise tuning of the interlayer spacing. The pioneering study by Lukatskaya *et al.* [71] revealed that multiple cations, including Li^+, Na^+, Mg^{2+}, K^+, NH_4^+, and Al^{3+}, can spontaneously intercalate into Ti_3C_2, highlighting new opportunities for developing improved intercalation electrodes in rechargeable batteries. As illustrated in Fig. 6(a), Li *et al.* [72] provided a comprehensive summary of the key factors governing ion intercalation in MXenes. Specifically, a smaller effective ionic size and higher valence state facilitate greater ion accommodation within the interlayer space. Additionally, the type of MXene is closely related to ion intercalation. Variations in chemical composition lead to different electronic distributions, interlayer interaction strengths, and lattice parameters, all of which ultimately affect the E_{ads} and diffusion barrier of the intercalated ions. Beyond these intrinsic factors, the solvation/desolvation effects of ions render the choice of solvent a critical factor in determining ion transport and intercalation kinetics. In a study by Subramanyan *et al.* [73], Na^+ intercalation in $V_4C_3T_x$ MXene was found to proceed more efficiently in ester-based electrolytes, where the diffusion kinetics are faster compared with those in the tetraethylene glycol dimethyl ether/tetraglyme (TEGDME)-based electrolytes. Recently, Yin *et al.* [74] conducted a systematic study on the intercalation of diverse metal cations (including Li^+, Na^+, K^+, Mn^{2+}, Zn^{2+}, Mg^{2+}, and Al^{3+}) into MXenes and their influence on electrochemical performance. As shown in Figs. 6(b) and (c), cations in $Ti_3C_2T_x$ can occupy Top, Hollow, or Mid sites, with the preferred site varying across different ion species according to formation energy calculations. Notably, Mn^{2+}-intercalated $Ti_3C_2T_x$ exhibits superior cycling stability and overall electrochemical performance compared with the pristine structure.

Although metal cation intercalation is a conventional strategy for tuning the interlayer spacing of MXenes, the limited expansion achievable due to the relatively small ionic radius often fails to meet the demands of advanced applications. To overcome this limitation, researchers have been exploring alternative intercalants capable of providing larger interlayer distances. Notably, incorporating nonmetallic ions and organic molecules into MXene interlayers has been recognized as an effective means to enlarge the interlayer spacing and broaden the possibilities for structural engineering. As reported by Ji *et al.* [25], the interlayer spacing of $Ti_3C_2T_x$ increased from 1.03 to 1.45 nm, and that of $Mo_2TiC_2T_x$ from 1.26 to 2.14 nm [Fig. 6(d)], through the intercalation of n-hexylamine/N-methylformamide (HA/NMF) molecules. A quantitative correlation exists between the intercalated molecules and the resulting interlayer spacing. Arole *et al.* [75] tuned the interlayer spacing of multilayer $Ti_3C_2T_z$ (ML-$Ti_3C_2T_z$) by introducing intercalants of various sizes, including lithium chloride (LiCl), sodium chloride (NaCl), urea (CH_4N_2O), dimethyl sulfoxide (DMSO), and tetrabutylammonium hydroxide (TBAOH). X-ray diffraction (XRD) patterns of intercalated ML-$Ti_3C_2T_z$ were systematically collected to investigate the structural evolution induced by intercalation [Fig. 6(e)]. The XRD analysis reveals that intercalation with different species leads to a leftward shift of the (002) peak of ML- $Ti_3C_2T_z$, indicating an increase in the interlayer spacing. Owing to its relatively large molecular size, TBAOH causes the (002) peak of ML-$Ti_3C_2T_z$ to shift from 7.2° to 5.1°. As depicted in Fig. 6(f), the linear fit ($R^2 = 0.9028$) indicates a strong positive correlation between intercalant size and interlayer spacing. This implies that the interlayer spacing in ML-$Ti_3C_2T_z$ can be accurately predicted based on the size of the intercalants, thereby enabling the rational design of MXene properties for diverse applications. To gain deeper insights into the role of guest molecules in intercalation and chemical modification, Wei *et al.* [76] investigated the interaction mechanism between $[Emim]^+$ and bilayer MXene. Based on the appropriate size and electronic potential maps of $[Emim]^+$ [Fig. 6(g)], it was found to intercalate into Ti_2CO_2 bilayers and exhibit a stable adsorption configuration, maintaining an interlayer distance of 8.1 Å. Furthermore, quantitative Bader charge analysis revealed that $[Emim]^+$ acquires 0.054 e^- from the Ti_2CO_2 bilayer. This mild charge transfer suggests that the insertion of $[Emim]^+$ does not drastically distort the MXene bilayer, allowing it to maintain a stable bilayer distance. Meanwhile, diffusion kinetics studies reveal that the diffusion barriers of various metal ions within the pillared structures formed by guest molecule intercalation are significantly lower than those in the pristine Ti_2CO_2 bilayer. This improvement is primarily due to the guest molecules effectively supporting the interlayer spacing and weakening the binding energy of MI. Consequently, the facilitated ion migration leads to enhanced diffusion kinetics and improved rate capability of the battery.

2.5 Heterogeneous structure engineering

The emerging class of van der Waals (vdW) heterostructures, composed of diverse 2D materials, is distinguished by its ability to integrate individual advantages and generate synergistic effects. The rational design of MXene-based heterostructures is particularly promising, as it can significantly enhance ion and electron transport within electrodes while maintaining structural stability [35]. Consequently, such architectures offer novel properties and unexpected opportunities for the design and optimization of advanced electrode materials. At present, a wide range of 2D materials, including graphene [77, 78], transition metal dichalcogenides (TMDs) [79, 80], and transition metal oxides (TMOs) [81], have been employed to construct MXene-based heterostructures. These structures have demonstrated

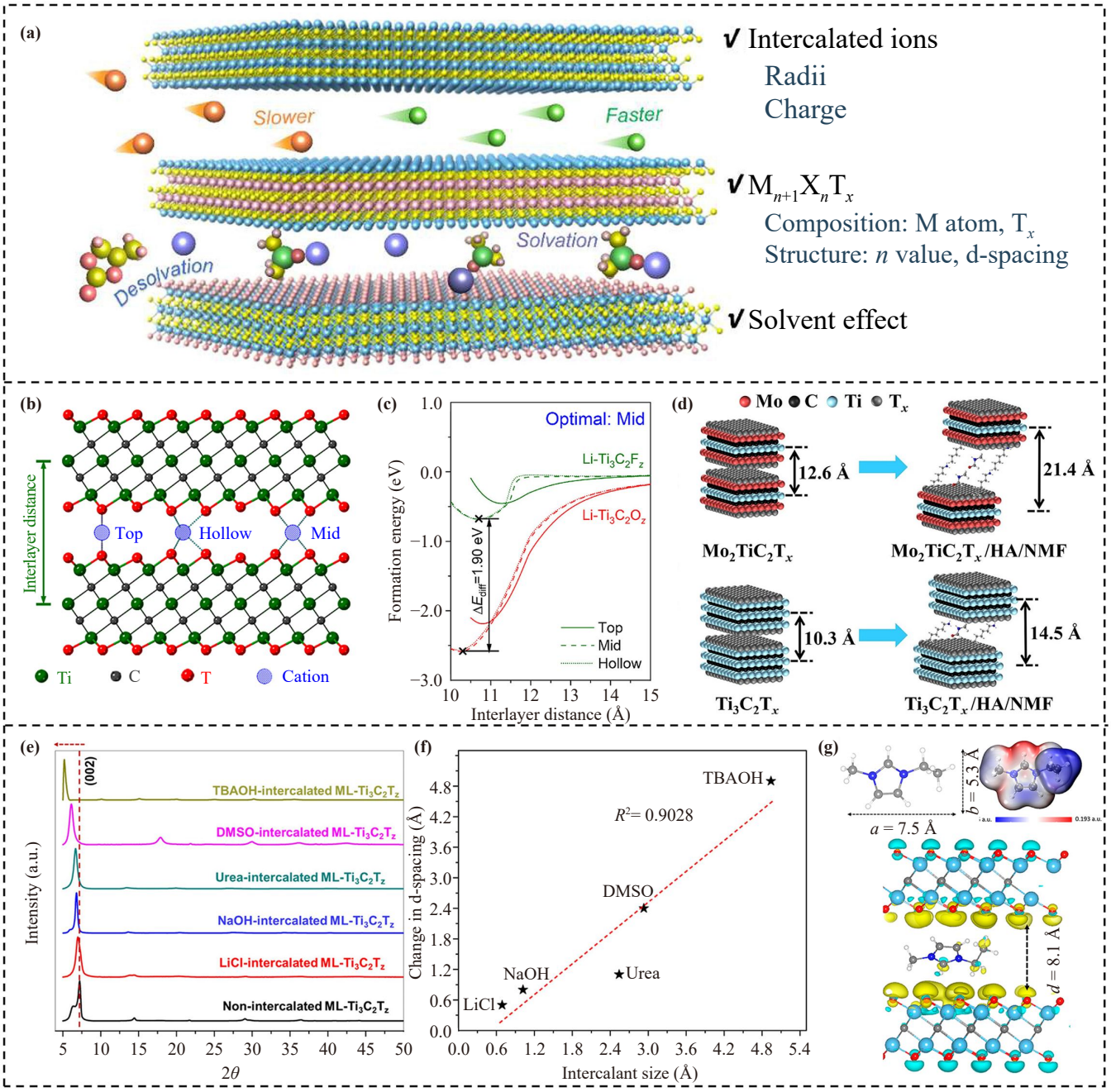

Fig. 6 **(a)** Schematic diagram of factors affecting ion intercalation. Reproduced with permission from Ref. [72]. Copyright © 2024 Elsevier. **(b)** Three possible configuration diagrams of cation embedding in $Ti_3C_2T_x$ bilayer. **(c)** The function diagram of the formation energy and interlayer distance of the $Ti_3C_2T_x$-Li system shows the optimal configuration of cation intercalation. Reproduced with permission from Ref. [74]. Copyright © 2024 Elsevier. **(d)** Interlayer spacing of $Ti_3C_2T_x$ and $Mo_2TiC_2T_x$ bilayer before and after HA/NMF intercalation. Reproduced with permission from Ref. [25]. Copyright © 2025 Elsevier. **(e)** XRD patterns of intercalated ML-$Ti_3C_2T_z$ MXene showing a leftward shift of the (002) reflection. **(f)** Linear fitting of intercalant size and interlayer spacing in MXenes bilayers. Reproduced with permission from Ref. [75]. Copyright © 2024 American Chemical Society. **(g)** Size and ESP of the $[Emim]^+$, and charge density difference (CDD) maps of a Ti_2CO_2-$[Emim]^+$ bilayer. Reproduced with permission from Ref. [76]. Copyright © 2022 American Chemical Society.

outstanding electrochemical performance as electrode materials.

Figure 7(a) presents the schematic structure of the MXene/graphene heterostructure, where Aierken *et al.* [82] employed theoretical calculations to reveal that the M_2CT_2 (M = Sc, Ti, V; T = OH, O)/graphene heterostructures undergo only slight structural modifications. Moreover, the negative binding energies indicate

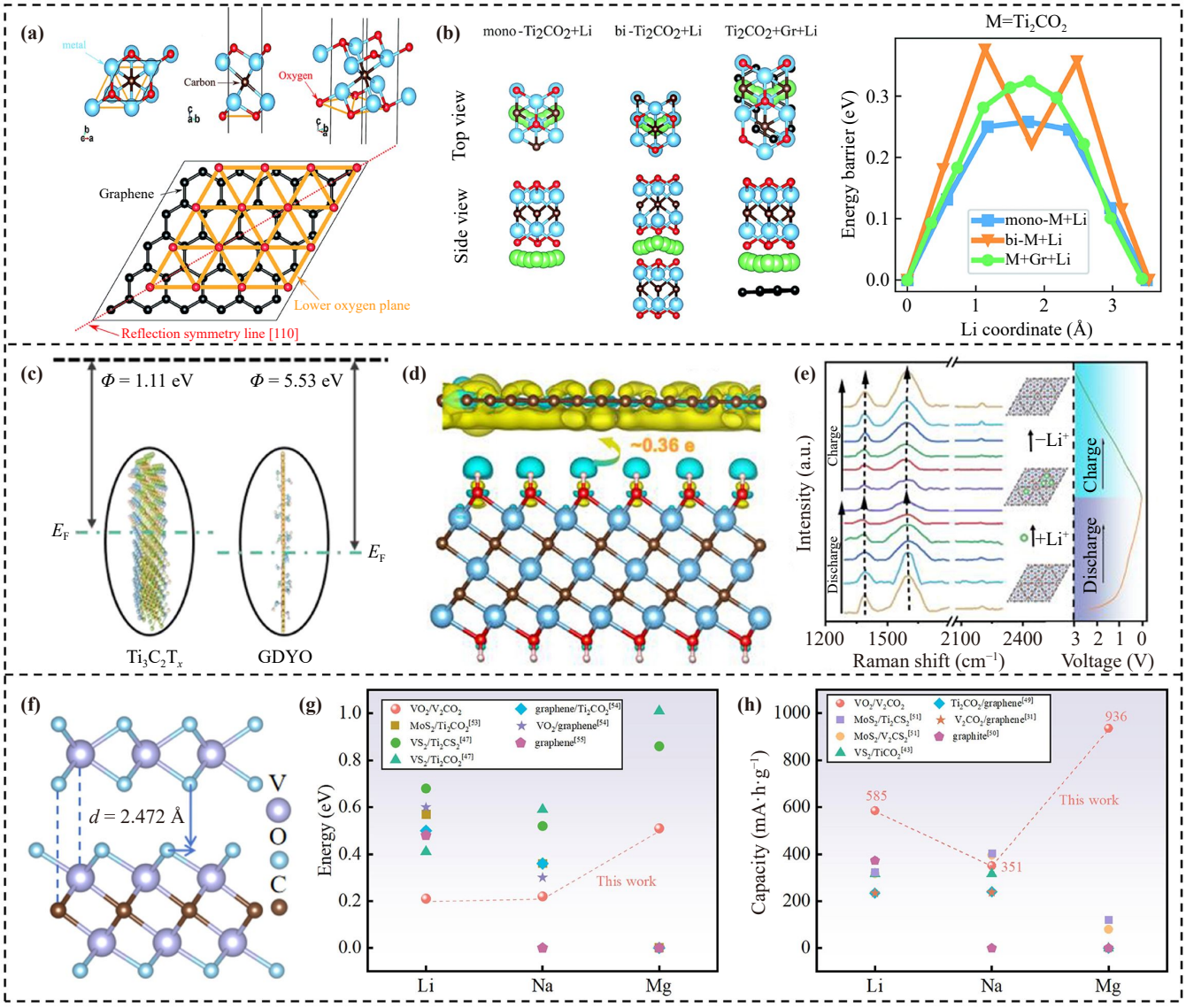

Fig. 7 **(a)** Typical example structure of Ti_2CO_2 MXene and simplified example of the M_2CT_2/graphene heterostructure in its ground state stacking. **(b)** Top and side views of the most favorable Li diffusion paths and corresponding energy profiles in Ti_2CO_2 monolayers, Ti_2CO_2 bilayers, and Ti_2CO_2/graphene heterostructure systems. Reproduced with permission from Ref. [82]. Copyright © 2018 Royal Society of Chemistry. **(c)** Electrostatic potential difference of $Ti_3C_2T_x$ and GDYO. **(d)** The CDD plot at the interface. **(e)** In situ Raman spectra of $Ti_3C_2T_x$/GDYO during charging and discharging processes. Reproduced with permission from Ref. [83]. Copyright © 2023 Elsevier. **(f)** The interlayer spacing generated by the optimized VO_2/V_2CO_2 heterostructure. **(g)** Diffusion barriers and **(h)** capacity of Li, Na, and Mg in VO_2/V_2CO_2 and other 2D materials. Reproduced with permission from Ref. [84]. Copyright © 2025 Elsevier.

that these heterostructures are more stable than their separated phases. In particular, Ti_2CO_2/graphene offers a compromise between capacity and kinetics, as it exhibits the lowest diffusion barrier among the considered systems, even lower than that of graphene [Fig. 7(b)]. In the work of Wang *et al.* [83], ultrathin 2D graphdiyne oxide (GDYO) was innovatively intercalated into $Ti_3C_2T_x$ to construct a sandwich-like heterostructure, leading to a significant expansion of the interlayer spacing. As illustrated in Fig. 7(c), the difference in work functions reveals that electrons were transferred across the interface toward GDYO under the driving force of the potential difference. Figure 7(d) reveals that approximately 0.36 e^- is transferred from $Ti_3C_2T_x$ to GDYO, which verifies the occurrence of electronic coupling in this heterostructure. Furthermore, owing to interlayer expansion and structural evolution during the lithiation process, slight redshifts of the D and G bands are observed for $Ti_3C_2T_x$/GDYO, accompanied by a decrease in the intensities of the G band and alkyne-

related peaks [Fig. 7(e)]. During the subsequent charging process, the peak intensities recover to their initial states, demonstrating the excellent electrochemical reversibility and structural stability of $Ti_3C_2T_x$/GDYO. This unique architecture endows the material with enhanced electronic conductivity and stronger adsorption, while simultaneously accelerating reaction kinetics during cycling. In a recent study, Ji *et al.* [84] constructed a van der Waals heterostructure composed of VO_2/V_2CO_2. Among the six possible configurations considered, the most stable one is shown in Fig. 7(f). This structure features the shortest interlayer spacing, which strengthens the van der Waals interactions and consequently enhances the structural stability, as indicated by the most negative formation energy. In addition, AIMD simulations performed at 300 K revealed only minor structural fluctuations, while the overall integrity of the heterostructure was preserved. This outstanding thermal stability under room-temperature conditions is of particular significance, as it underpins the long-term operational stability required for practical battery applications. Electronic characteristic analyses confirm the superior metallic nature of the heterostructure, suggesting high carrier density and favorable electrical conductivity. The migration kinetics results [Fig. 7(g)] reveal that the diffusion barriers of Li, Na, and Mg ions within the heterostructure interlayer are relatively low, which contributes to its superior rate capability. As presented in Fig. 7(h), the VO_2/V_2CO_2 heterostructure delivers impressive theoretical capacities, with the Mg-ion system achieving as high as 936 $mA{\cdot}h{\cdot}g^{-1}$, surpassing other 2D materials and underscoring its strong potential as an advanced anode candidate.

3 Applications to electrode materials of rechargeable battery

From portable electronic devices to electric vehicles, rechargeable batteries have become a cornerstone of modern green living and technological progress. However, the limitations of traditional electrode materials in terms of energy density, cycle life, environmental impact, and cost of use are becoming increasingly prominent [85]. Consequently, designing and developing next-generation high-performance electrode materials is an urgent yet challenging task. Benefiting from the distinctive electronic structures and superior physicochemical characteristics, MXene materials have been recognized as highly promising candidates for rechargeable battery electrodes. Additionally, as discussed in the previous sections, various effective modification strategies have further expanded their applicability and significantly enhanced their overall performance. In the following sections, we will discuss the applications of MXene-based materials in different types of rechargeable batteries.

3.1 Lithium-ion batteries (LIBs)

LIBs, as high-performance secondary batteries, currently dominate the commercial market due to their technological maturity. With the continuous upgrading of industrial products, increasing demands have been placed on the safety, energy density, and fast charge-discharge capability of LIBs. An ideal LIB is expected to possess high storage capacity, outstanding cycling stability, and reliable rate performance. Among the numerous influencing factors, the electrochemical behavior is most strongly dictated by the properties of the electrode materials. Despite being the most widely used anode material in LIBs, graphite is constrained by its low theoretical capacity (372 $mA{\cdot}h{\cdot}g^{-1}$) [86] and lithiation potential (<0.2 V) [87], which make it susceptible to lithium dendrite formation and consequently raises safety concerns during cycling. Since the discovery of MXenes, extensive theoretical studies have been devoted to exploring their feasibility as anode materials for LIBs.

The investigation of Li storage performance in $Ti_3C_2T_x$ through theoretical calculations was initiated by Naguib *et al.* [8], who employed DFT to demonstrate that Ti_3C_2 MXene possesses excellent electronic conductivity and offers a theoretical Li storage capacity of 320 $mA{\cdot}h{\cdot}g^{-1}$, which is close to the value of graphite (372 $mA{\cdot}h{\cdot}g^{-1}$). Building on this foundation, the study by Tang *et al.* [45] revealed that bare Ti_3C_2 exhibits a remarkably low diffusion barrier of 0.07 eV, significantly lower than that of graphite (0.3 eV), highlighting its potential as an anode material for LIBs. The specific capacity of MXenes is also affected by factors such as the molar mass of their constituent elements and the thickness of the atomic layers. Eames *et al.* [88] further investigated a broader range of transition-metal-based MXenes as anode materials for LIBs, including Sc, Ti, V, Cr, Zr, Nb, Mo, Hf, and Ta. It was found that MXenes containing lighter 3d elements (Sc, Ti, V, Cr) possess larger theoretical capacities compared with those incorporating heavier 4d/5d metals (Zr, Nb, Mo, Hf, Ta), reflecting the inverse relationship with their molar mass. Motivated by the remarkable Li-storage performance of lighter 3d metals (Sc, Ti, V, Cr), Zhao *et al.* [89] explored a variety of MXene architectures (M_2C, MC_2, M_2N, MN_2) through theoretical screening and prediction, as illustrated in Fig. 8(a). Their findings culminated in the establishment of a universal functional relationship, which offers a broadly applicable principle to guide the development of high-capacity electrode materials. Following systematic screening involving stability, electronic properties, diffusion barriers, OCV calculations, and theoretical capacity evaluations, Ti_2N (975 $mA{\cdot}h{\cdot}g^{-1}$) and V_2N (924 $mA{\cdot}h{\cdot}g^{-1}$) exhibited storage capacities far exceeding those of graphite, confirming their significant potential as anodes for LIBs. Importantly, by combining Figs. 8(b) and (c), a relationship

between the d-band center and concentration can be established. According to this correlation, calculating the d-band center alone is sufficient to determine the E_{ads} of a single Li ion for unknown MXenes, thus enabling predictions of their theoretical capacity. This provides a powerful descriptor to accelerate the discovery of MXene anodes for LIBs.

Meanwhile, various modified MXene materials have been extensively investigated as LIBs electrodes, exhibiting excellent electrochemical performance. However, pristine MXenes are intrinsically unstable and tend to be terminated by functional groups. Among these, O- and S-functionalized MXenes have shown particular promise as electrode materials [90]. Considering the experimentally observed surface inhomogeneity of MXenes, Wei *et al.* [91] systematically examined the interactions and cooperative effects between O and S mixed terminations on V_2C. Their findings indicate that V_2CT_x maintains good metallic conductivity across different mixing ratios, primarily due to the d orbitals of V atoms. In particular, $V_2CO_{2/3}S_{4/3}$ delivers a low OCV of 0.29 V along with a theoretical capacity of 729 $mA{\cdot}h{\cdot}g^{-1}$, as summarized in the voltage-capacity plot [Fig. 8(d)], underscoring the extraordinary potential of functional groups in tailoring the properties of MXenes. Compared with single-transition-metal MXenes, the emergence of double-transition-metal MXenes (DTMs) alleviates the limitations imposed by the higher molar mass of early transition metals, thereby exhibiting higher theoretical capacity and greater potential for applications in electrochemical energy storage. Zhou *et al.* [92] reported WCrC and MoWC DTMs by substituting Mo/Cr for W, yielding materials with excellent electronic conductivity [Fig. 8(e)]. Their study demonstrated that the synergistic effect of dual transition metals, combined with relatively low molar mass, not only provided higher Li storage capacities (648.81 $mA{\cdot}h{\cdot}g^{-1}$ for WCrC and 551.82 $mA{\cdot}h{\cdot}g^{-1}$ for MoWC) but also resulted in remarkably low diffusion barriers (0.045 eV for WCrC and 0.046 eV for MoWC), as depicted in Fig. 8(f). Additionally, the discovery that highly electronegative metals in DTMs weaken the metal–carbon bonds, thus potentially enhancing Li adsorption, provides a means to tune the metal-ion adsorption behavior of MXenes and promotes the advancement in MXene surface engineering. Black phosphorus (BP), as indicated by theoretical studies, possesses characteristics beyond the reach of graphene, TMDs, and other 2D materials [93]. Building on this, Saharan *et al.* [94] designed a stable BP/MXene heterostructure that combines the unique strengths of the two materials while partially mitigating self-restacking issues. It is evident in Fig. 8(g) that BP/Ti_3C_2 and $BP/Ti_3C_2N_2$ can accommodate up to seven and six complete layers of Li, respectively, which surpasses the theoretical capacity of their individual components as LIBs cathodes. In terms of migration capability, BP/Ti_3C_2 and $BP/Ti_3C_2N_2$ demonstrate very low diffusion barriers (0.020 eV and 0.2 eV, respectively) for Li ions along the considered pathways [Fig. 8(h)], which is highly beneficial for achieving fast ion transport and excellent rate performance.

3.2 Lithium–sulfur (Li–S) batteries

As potential contenders for next-generation energy storage systems, Li–S batteries have been extensively investigated, primarily owing to their impressive energy density of 2600 $Wh{\cdot}kg^{-1}$, high theoretical capacity of up to 1675 $mA{\cdot}h{\cdot}g^{-1}$, and the abundance of sulfur resources [95, 96]. However, the advancement of Li–S batteries has been significantly hampered by several critical challenges, including the low electrical conductivity of sulfur cathodes, the shuttle effect of lithium polysulfides (LiPSs), and sluggish redox kinetics. To overcome these limitations, extensive research has focused on designing advanced cathode materials with both superior electrical conductivity and strong capability to immobilize LiPSs. This dual characteristic is crucial for promoting rapid charge transfer while alleviating the shuttle effect by restricting the dissolution and diffusion of LiPSs. Benefiting from the synergy between high intrinsic conductivity and abundant surface activity, MXenes demonstrate outstanding potential as sulfur hosts in Li–S batteries.

MXenes possess abundant surface functional groups that play a crucial role in anchoring LiPSs and suppressing the shuttle effect. In 2017, Rao *et al.* [97] systematically investigated the performance of bare Ti_2C and Ti_2C functionalized with F, O, and OH in Li–S battery systems. As shown in the optimized structure of Fig. 9(a), the S atoms in LiPSs are dispersed on the bare Ti_2C surface due to the strong interactions between S and Ti atoms, indicating that bare Ti_2C cannot serve as an ideal anchoring material. In contrast, surface functionalization mitigates the strong Ti–S interactions, enabling efficient trapping of LiPSs without decomposition and underscoring its significance in enhancing the anchoring ability of MXenes. In addition to the common F, O, and OH terminations, Wang *et al.* [98] further explored the anchoring effects of Ti_3C_2 functionalized with N, O, F, S, and Cl on LiPSs, all of which retained the same metallic conductivity as bare Ti_3C_2 [Fig. 9(b)]. As illustrated in Fig. 9(c), the order of the adsorption capacity of $Ti_3C_2T_2$ for LiPSs is as follows: S > O > N > F > Cl. Among these, $Ti_3C_2S_2$ and $Ti_3C_2O_2$ stand out with significantly enhanced binding strengths, highlighting their potential as competitive sulfur cathode hosts. Compared with conventional single-metal MXenes, the incorporation of multiple metal sites in HE-MXenes triggers a cocktail effect, thereby endowing them with potentially distinctive catalytic properties. Xu *et al.* [99] designed a $TiVNbMoC_3$ HE-MXene with excellent structural compatibility as a platform for multi-active-center

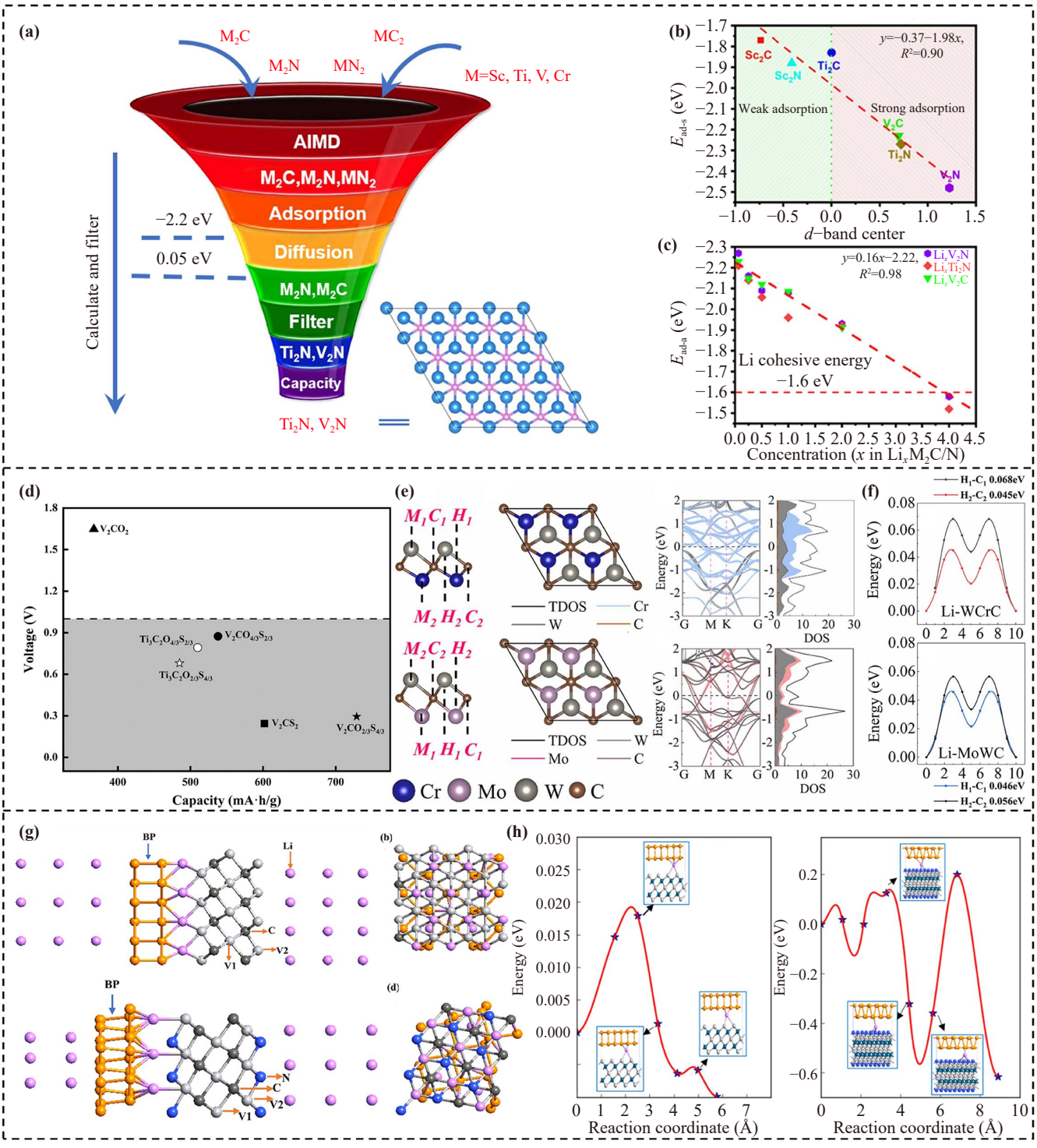

Fig. 8 **(a)** Structure screening flowchart. **(b)** The relationship between the d-band centers of different structures and the E_{ads} of a single Li ion. **(c)** The relationship curve between Li adsorption concentration and the average E_{ads}, where x represents the concentration. Reproduced with permission from Ref. [89]. Copyright © 2021 Elsevier. **(d)** Schematic diagram of theoretical capacity and average OCV of different anode materials. Reproduced with permission from Ref. [91]. Copyright © 2024 Elsevier. **(e)** Structural configurations and corresponding calculated band structures and DOS of WCrC (top) and MoWC (bottom) monolayers. **(f)** The Li migration path with the lowest diffusion energies on the WCrC and MoWC monolayer. Reproduced with permission from Ref. [92]. Copyright © 2023 IOP Publishing. **(g)** BP/MXene (V_3C_2, $V_3C_2N_2$) heterostructure after Li intercalation. **(h)** Relative energy profiles along the diffusion routes for Li atom on BP/MXene (V_3C_2, $V_3C_2N_2$) heterostructure. Reproduced with permission from Ref. [94]. Copyright © 2023 American Chemical Society.

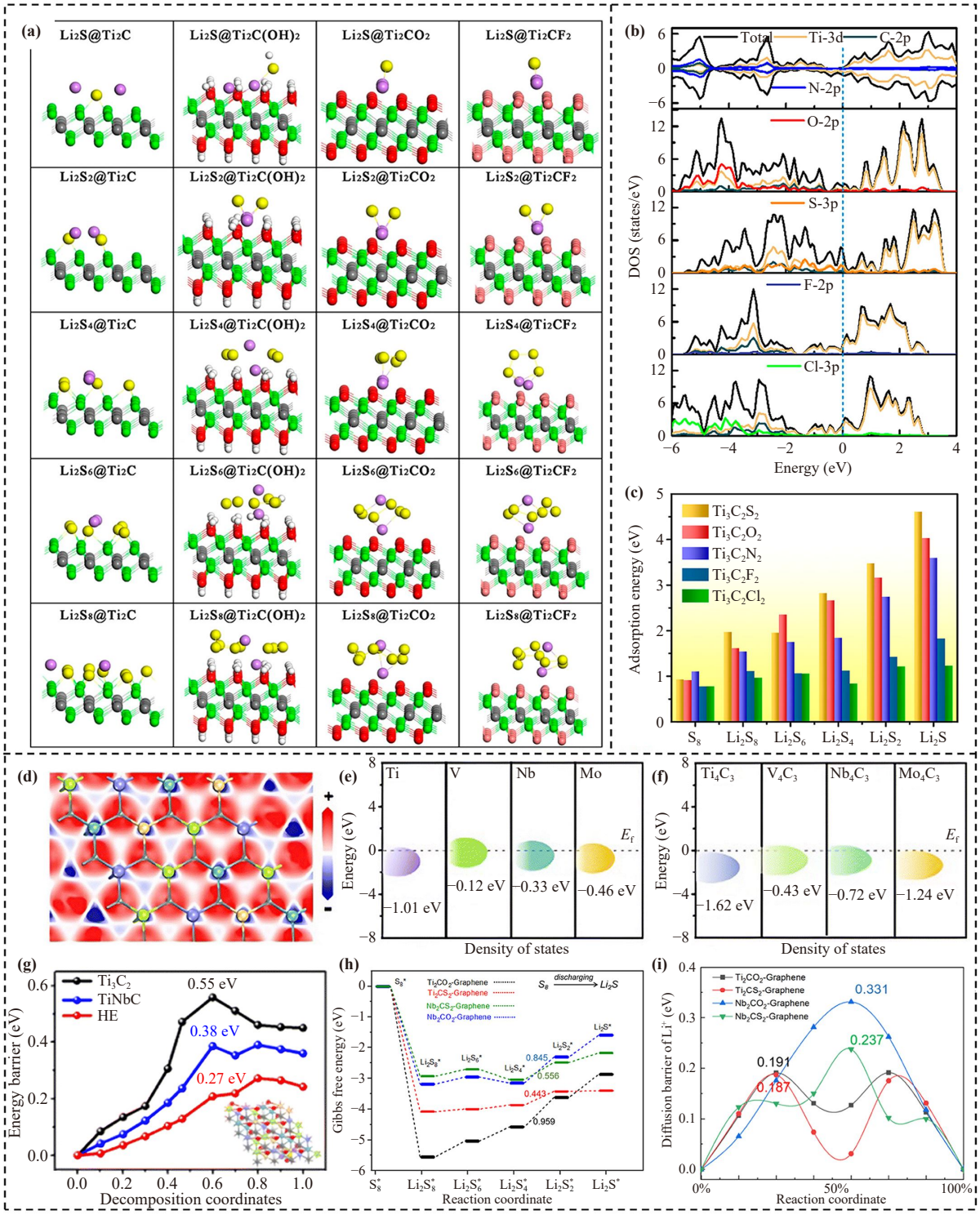

Fig. 9 **(a)** Optimized adsorption configurations of various LiPSs on Ti_2C, $Ti_2C(OH)_2$, Ti_2CO_2, Ti_2CF_2. Reproduced with permission from Ref. [97]. Copyright © 2017 American Chemical Society. **(b)** The calculated DOS of the $Ti_3C_2T_2$ (T = N, O, F, S, and Cl). **(c)** Adsorption energies of S_8 and Li_2S_n on $Ti_3C_2T_2$. Reproduced with permission from Ref. [98]. Copyright © 2019 American Chemical Society. **(d)** The electron density distribution of $TiVNbMoC_3$ HE-MXene system. The calculated d-band centers of different metal atoms in **(e)** $TiVNbMoC_3$ HE-MXene and **(f)** the corresponding single-metal MXenes. **(g)** Energy barriers for Li_2S dissociation on Ti_3C_2, TiNbC and HE-MXene surface. Reproduced with permission from Ref. [99]. Copyright © 2024 Royal Society of Chemistry. **(h)** Gibbs free energy barriers of SRR on MXene-Graphene heterostructures. **(i)** Diffusion energy barriers of Li ion the heterostructure surfaces. Reproduced with permission from Ref. [100]. Copyright © 2024 American Chemical Society.

synergistic engineering in Li–S batteries. Notably, the significant lattice distortion within this configuration triggers a redistribution of surface charge density [Fig. 9(d)]. The study of electronic properties demonstrates that the DOS of $TiVNbMoC_3$ is located closer to Fermi level than that of Ti_3C_2 and TiNbC, leading to moderate E_{ads} and superior catalytic activity. In addition, PDOS analysis shows a pronounced shift of the transition-metal d-band centers toward Fermi level, exceeding those of the single-metal counterparts Ti_4C_3, V_4C_3, Nb_4C_3, and Mo_4C_3 MXenes. This observation suggests that the synergistic interaction among multiple active sites in HE-MXene contributes to the optimization of the d-band center [Figs. 9(e) and (f)]. Further studies demonstrated that HE-MXene reduces the decomposition barrier of Li_2S, which in turn facilitates faster LiPSs conversion kinetics during the charge-discharge process [Fig. 9(g)]. Moreover, constructing heterostructures as sulfur cathode hosts is considered an effective strategy, as it not only enhances interlayer structural stability but also strengthens the anchoring of polysulfides, ultimately improving the electrocatalytic performance in Li–S batteries. Ge *et al.* [100] reported the catalytic effects of four different MXene–graphene heterostructures on the conversion of S_8 to Li_2S during discharge process. The Gibbs free energy change (ΔG) profiles of the sulfur reduction reaction (SRR) are depicted in Fig. 9(h), where the step from Li_2S_4 to Li_2S_2 exhibits the largest positive ΔG barrier, identifying it as the rate-limiting step. More importantly, when compared with the 1.07 eV barrier reported for the rate-limiting step of the SRR on graphene [101], the calculated results demonstrate that these heterostructures exhibit superior catalytic activity toward SRR. Similarly, Li diffusion on the cathode host plays a crucial role in determining the charging dynamics of Li–S batteries. As exhibited in Fig. 9(i), the calculated diffusion energy barriers reveal that Li migration on the Ti_2CS_2-graphene heterostructure possesses a relatively low barrier, which is favorable for enhancing the charging rate. A comprehensive comparison between pristine graphene and MXene materials confirms the synergistic effect arising from their integration. Consequently, under the premise of effectively suppressing the shuttle effect, the Ti_2CS_2-graphene heterostructure demonstrates enhanced catalytic activity toward SRR and significantly improved charge-discharge kinetics.

3.3 Lithium–oxygen (Li–O_2) batteries

Rechargeable Li–O_2 batteries, with an ultrahigh theoretical energy density of 3500 $W{\cdot}h{\cdot}kg^{-1}$ [102], are regarded as strong candidates for next-generation energy storage systems. From an electrochemical perspective, their charge-discharge process primarily involves the reversible formation and decomposition of lithium peroxide ($2Li + O_2 + 2e^- \rightleftharpoons Li_2O_2$). However, several challenges hinder the commercialization of Li–O_2 batteries, including high overpotential, slow ORR/OER kinetics, as well as the insulating and insoluble nature of the discharge products (Li_2O_2). Consequently, the exploration of novel oxygen electrode catalysts is of critical importance for enhancing electrochemical properties, reducing the overpotential, and achieving more efficient reaction pathways.

Functionalization has emerged as an effective strategy to improve the catalytic activity of MXene materials. In a recent study, Wei *et al.* [103] reported a synergistic engineering approach that integrates the physical structure and surface chemistry of MXenes, thereby delivering exceptional bifunctional electrocatalytic activity. This design significantly accelerates ORR/OER kinetics in Li–O_2 batteries, showcasing great potential as a next-generation power source for electric vehicles. In this study, the conventional layered framework of MXenes was reconstructed into hollow spheres and entangled wires. Such a structural transformation substantially increased the surface area and exposed more interlayer sites, thereby facilitating rapid charge transfer during ORR/OER processes. As displayed in Figs. 10(a)–(c), calculation results confirmed that surface terminations (–O/–F/–OH) can markedly reduce the reaction barriers, thereby lowering the ORR/OER overpotentials, suppressing side reactions, and enhancing catalytic kinetics. In particular, O-functionalized $Ti_3C_2O_2$ exhibited the lowest overpotential compared to bare Ti_3C_2 [Figs. 10(b) and (c)], which enhanced the reversibility of the ORR/OER while ultimately enabled prolonged cycling stability. Zhao *et al.* [104] employed a CO_2-assisted strategy to embed Se single atoms (Se-SAs) into Ti vacancies on the surface of Ti_3C_2, breaking the structural symmetry of MXene nanosheets and markedly enhancing the catalytic activity of the electrode. The evident charge transfer in Fig. 10(d) highlights strong interactions between Se and Ti. Combined with a low adsorption energy (E_{ads} = –0.98 eV), these results indicate that Se-SAs act as catalytic centers, enhancing charge transfer and substantially strengthening the intrinsic LiO_2 adsorption ability, which is beneficial for accelerating the ORR in Li–O_2 batteries. In stark contrast to bare Ti_3C_2, SeSA-Ti_3C_2 exhibited ORR and OER overpotentials of 0.29 and 0.59 V, respectively, which are much lower than the overpotentials of 0.54 and 1.06 V for Ti_3C_2 [Fig. 10(e)]. This finding underscores the crucial role of SAs Se active sites in reducing the overpotentials associated with both the formation and decomposition of Li_2O_2. In heterogeneous catalysis, limited adsorption behaviors of reaction intermediates on single-metal MXenes often restrict charge transfer. The introduction of a secondary metal can effectively strengthen intermediate adsorption by modulating the electronic structure of the metal sites within the lattice. For example, Ren *et al.* [105] innovatively designed a Ce-doped Ti-vacancy-engineered $Ti_3C_2T_x$

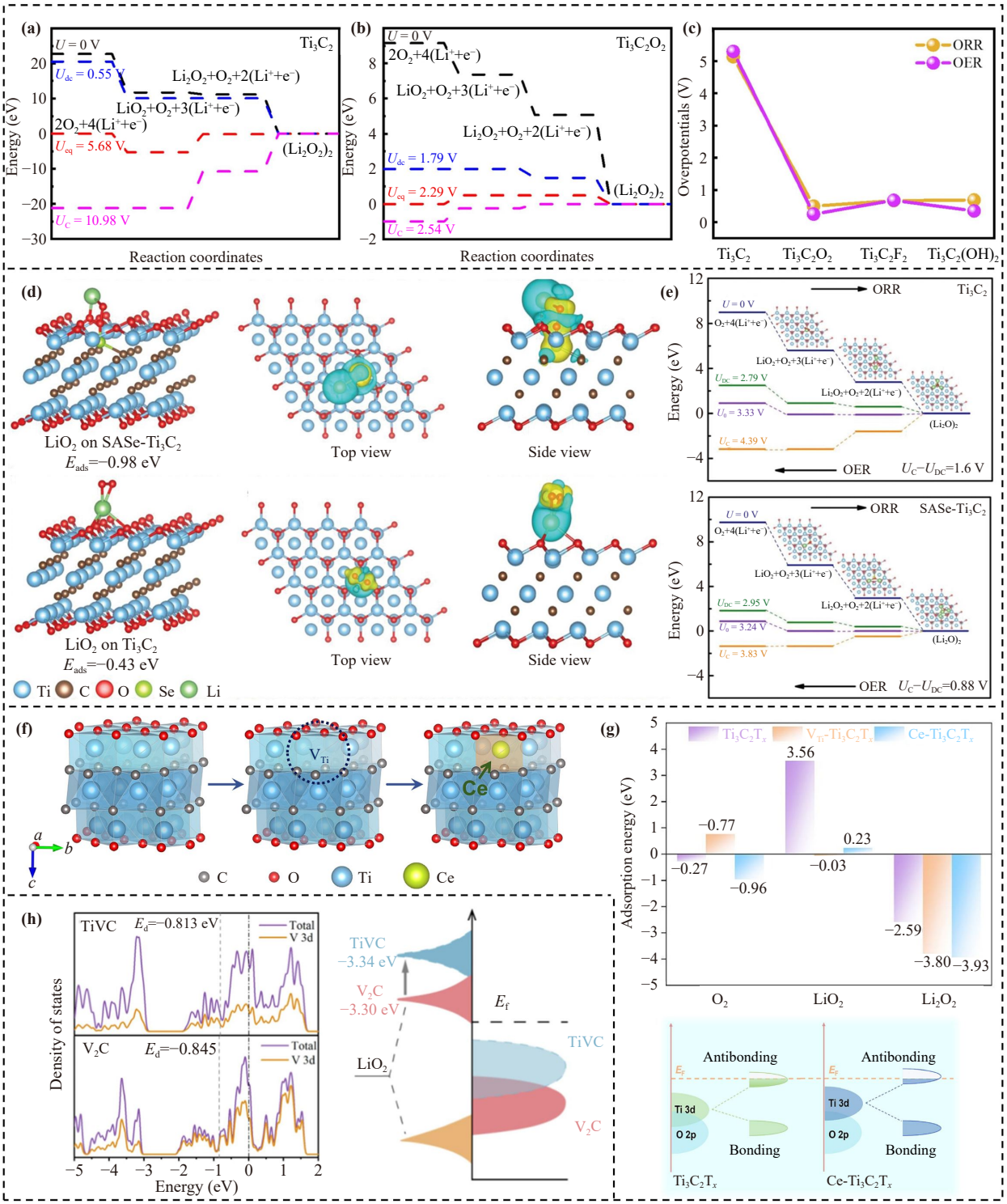

Fig. 10 Free energy diagrams of **(a)** Ti_3C_2, **(b)** $Ti_3C_2O_2$, regarding discharge and charge simulations. **(c)** The overpotential of Ti_3C_2, $Ti_3C_2T_2$ (T = O, F and OH) over ORR and OER process. Reproduced with permission from Ref. [103]. Copyright © 2026 Elsevier. **(d)** Optimized structure, E_{ads} and the corresponding CDD of LiO_2 on SASe-Ti_3C_2 and Ti_3C_2. **(e)** The calculated free energy diagrams for the ORR/OER reactions on the active surface of Ti_3C_2 and SASe-Ti_3C_2. Reproduced with permission from Ref. [104]. Copyright © 2021 John Wiley and Sons. **(f)** Schematic diagram of Ce anchoring at $Ti_3C_2T_x$ defect site in modulation process. **(g)** E_{ads} of different Li species on $Ti_3C_2T_x$, V_{Ti}-$Ti_3C_2T_x$, and Ce-$Ti_3C_2T_x$ (top), and energy-level splitting of Ti 3d orbitals in pristine $Ti_3C_2T_x$ and Ce-$Ti_3C_2T_x$ (bottom). Reproduced with permission from Ref. [105]. Copyright © 2025 Elsevier. **(h)** The DOS of TiVC and V_2C, accompanied by a schematic illustration of the bond formation between the valence bands of adsorbed LiO_2 and the d-states of TiVC and V_2C. Reproduced with permission from Ref. [106]. Copyright © 2024 Elsevier.

bifunctional catalyst [Fig. 10(f)]. Calculations of E_{ads} in Fig. 10g indicate that the superior adsorption of O_2 and Li_2O_2 on Ce-$Ti_3C_2T_x$ arises from a dual-regulation mechanism of the Ce–C–Ti triatomic bridge active center involving d-band center modulation and orbital hybridization coupling. Furthermore, a notable reduction in overpotentials (0.09 V for ORR and 0.20 V for OER) was achieved in Ce-$Ti_3C_2T_x$, which verifies the unique superiority of rare-earth doping in tuning the electronic occupancy of transition-metal d orbitals and introduces a new paradigm for the rational design of 2D catalytic materials. Similarly, exceptional electrochemical performance was observed for the bimetallic TiVC MXene synthesized by Liu *et al.* [106]. Figure 10(h) reveals electrons transfer from V to Ti within the Ti–C–V bonds, resulting in an upward shift of the V d-band center. This change strengthens the adsorption of the LiO_2 intermediate and accelerates the oxygen electrode reaction.

3.4 Non-lithium-ion batteries

The growing demand for large-scale energy storage has intensified reliance on lithium resources, leading to challenges for LIBs, including limited supply, safety hazards, and environmental impact. Given that sodium and potassium belong to the same group as lithium and possess similar physicochemical properties and storage mechanisms, SIBs and potassium-ion batteries (PIBs) are considered promising alternatives [107, 108]. Beyond SIBs and PIBs, multivalent metal ions such as Ca^{2+}, Mg^{2+}, Al^{3+} and Zn^{2+} are capable of transferring two or three electrons per ion, thereby providing higher energy density. These metal ion batteries (MIBs), characterized by high crustal abundance, low cost, and enhanced safety, are therefore regarded as strong candidates to address the resource and safety constraints posed by LIBs [109–111].

MXenes ($M_{n+1}X_n$) exhibit a diverse range of stoichiometries, such as M_2X, M_3X_2, and M_4X_3, offering abundant structural possibilities for the advancement of energy storage devices. A systematic study conducted by Guo *et al.* [112] examined $Ta_{n+1}C_n$ (n = 1, 2, and 3) [Fig. 11(a)] as anode candidates for alkali- and alkaline-earth- MIBs (Li, Na, K, Mg, and Ca). The calculated electronic structures demonstrate that $Ta_{n+1}C_n$ exhibits no gap between the conduction and valence bands, endowing it with excellent metallic character. An extremely low diffusion barrier ensures that alkali-metal ions can readily migrate across the $Ta_{n+1}C_n$ surface, enabling ultrafast charge-discharge and high performance. As summarized in Fig. 11(b), the theoretical storage capacity decreases with increasing n value and is negatively correlated with the ionic radius of the metal. These findings may provide theoretical guidance for designing novel MXene-based composite energy materials. Doping with other transition-metal elements of relatively low atomic mass, such as Sc, Ti, or Cr, can be regarded as an effective strategy to reduce energy barriers and enhance capacity for future applications and investigations. Bai *et al.* [113] analyzed Sc-doped $(Mo_{2/3}Sc_{1/3})_2C$ and $(Mo_{2/3}Sc_{1/3})_2CT_2$ (T = –O, –OH, and –F) double-transition-metal MXenes as high-performance electrode materials for ion batteries [Fig. 11(c)]. According to thermodynamic adsorption and structural dynamics simulations, the strong chemical reactivity between –OH/–F terminations and adsorbates can trigger structural decomposition. For this reason, these terminations were excluded from subsequent investigations of other electrochemical properties for various ion batteries. In particular, $(Mo_{2/3}Sc_{1/3})_2C$ and $(Mo_{2/3}Sc_{1/3})_2CO_2$ deliver superior metal-ion storage capacity, ideal OCV, and rapid ion-diffusion kinetics [Fig. 11(d)]. Janus materials, characterized by their asymmetric structures, have distinct chemical compositions on their two surfaces, thereby breaking the intrinsic symmetry and endowing the materials with novel properties. To advance research on Janus materials, Qin *et al.* [114] performed stability calculations, confirming the favorable thermodynamic and dynamic stability of Zr_2CSSe [Fig. 11(e)]. It is noteworthy that the asymmetric surface of the Janus Zr_2CSSe MXene generates a potential difference, creating an internal electric field that significantly improves ion transport and diffusion. As a substrate, Zr_2CSSe is capable of accommodating up to 24 Mg or Ca ions, corresponding to a theoretical capacity of 1052 $mA{\cdot}h{\cdot}g^{-1}$, which is considerably higher than that of traditional 2D materials. As shown in Fig. 11(f), low OCV values are retained even under the highest adsorption concentration, which guarantees the safety of batteries. By elucidating the role of structural asymmetry in modulating surface and interfacial properties, this study provides a framework for designing next-generation materials with tailored electrochemical functions. Currently, research interest has predominantly focused on carbide-related heterostructures, while comparatively fewer efforts have been directed toward nitride-based systems. To fill this gap, Ma *et al.* [115] proposed three optimal $Ti_3N_2T_2$ (T = F, O, OH)/VS_2 heterostructures with distinct terminations and systematically clarified the underlying mechanisms of charge transfer and ion diffusion. As seen in Fig. 11(g), the intrinsic metallicity ensures excellent electrical conductivity for all three heterostructures. To elucidate the interaction between the two monolayers within these heterostructures, the CDD and the planar-averaged CDD were investigated [Fig. 11(h)]. A redistribution of charge was observed in the interlayer region, confirming the existence of interaction and interlayer coupling between the monolayers. The electron localization function (ELF) map, presented in Fig. 11(i), revealed more distinct localized features in $Ti_3N_2(OH)_2/VS_2$, which implies higher charge density and stronger inter-

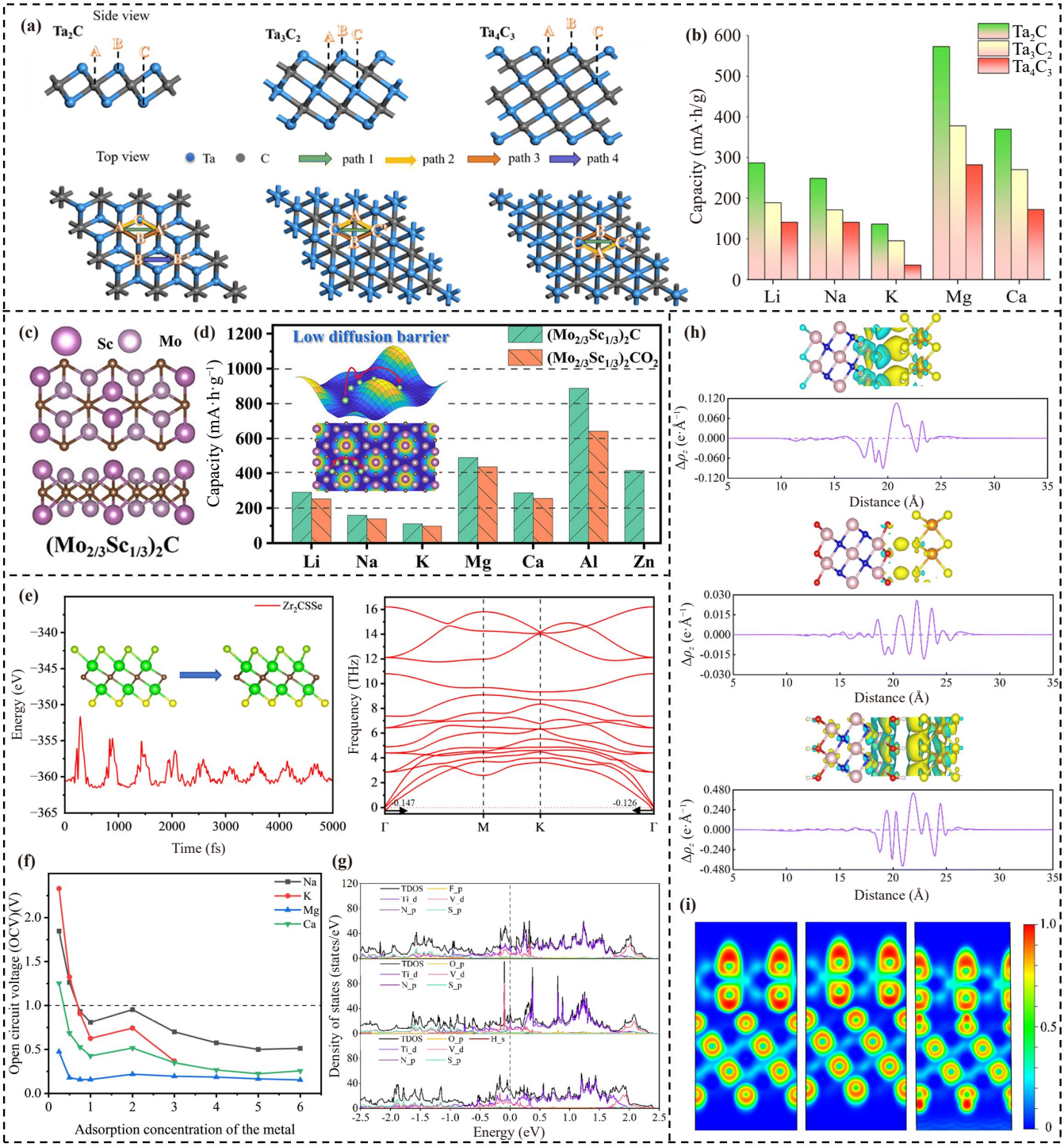

Fig. 11 **(a)** Top and side view structures of $Ta_{n+1}C_n$ (n = 1–3) MXenes. **(b)** Theoretical maximum capacities of various different MIBs. Reproduced with permission from Ref. [112]. Copyright © 2024 Royal Society of Chemistry. **(c)** Top and side views of the atomic structures of $(Mo_{2/3}Sc_{1/3})_2C$. **(d)** Theoretical capacities of $(Mo_{2/3}Sc_{1/3})_2C$ and $(Mo_{2/3}Sc_{1/3})_2CO_2$ for various MIBs. Reproduced with permission from Ref. [113]. Copyright © 2022 American Chemical Society. **(e)** Total energy evolution from AIMD simulation at 300 K and phonon dispersion curves of Zr_2CSSe MXene. **(f)** Variations of OCV with metal ions at different adsorption concentrations. Reproduced with permission from Ref. [114]. Copyright © 2025 Elsevier. **(g)** TDOS and PDOS of $Ti_3N_2F_2/VS_2$, $Ti_3N_2O_2/VS_2$ and $Ti_3N_2(OH)_2/VS_2$. **(h)** CDD and plane-averaged density of CDD in the Z direction and **(i)** ELF plots of the (110) slices of three heterostructures. Reproduced with permission from Ref. [115]. Copyright © 2024 Royal Society of Chemistry.

Table 1 Summary of key MXene properties, corresponding DFT methodologies, and their physicochemical significance under different application scenarios.

Application scenario	Property	DFT methodologies	Physicochemical significance
Intrinsic characteristics of MXene	Structure stability	Binding energy/Formation energy/AIMD/Phonon dispersion/Lattice parameter	Excellent stability is a critical factor governing long-term cycling performance.
	Electronic structure	Band structure/DOS	High metallic conductivity enables a high charge-carrier density, which is essential for superior rate capability.
	Theoretical storage capacity	E_{ads}/Maximum number of adsorbed ions	Strong adsorption capability provides abundant active sites, contributing to an enhanced theoretical storage capacity.
Application characteristics of anode materials for metal ion batteries	Anode voltage	OCV calculation	For metal-ion batteries, an OCV typically in the range of 0.1–1.0 V is desirable for balancing energy density and safety.
	The diffusion barrier of metal ions	Ion diffusion kinetics	A low diffusion energy barrier facilitates fast ion transport, which is critical for achieving high charge-discharge rate capability.
	Polysulfide adsorption	E_{ads}/CDD/Bader charge/ d-band center/	Moderate adsorption strength effectively suppresses LiPSs dissolution and mitigates the shuttle effect.
Application characteristics of cathode materials for Li–S batteries	Li-ion diffusion and Li_2S decomposition energy barrier	Reaction kinetics	Low energy barriers accelerate sulfur conversion reactions, enhancing charge-discharge kinetics.
	Sulfur reduction reaction	Gibbs free energy profile	Identifies the rate-determining step of SRR and evaluates the catalytic activity of electrode materials.
Application characteristics of cathode materials for Li–O_2 batteries	Intermediate adsorption	E_{ads}/CDD/Bader charge/ d-band center/	Moderate adsorption facilitates the formation and conversion of different Li–O intermediates.
	Overpotential	Gibbs free energy profile/ Voltage difference	Identifies the rate-determining step for ORR/OER and evaluates the catalytic activity of electrode materials.

actions. Taking into account structural integrity, strong adsorption capability, low diffusion barriers, high capacity, and appropriate OCV, $Ti_3N_2O_2/VS_2$ was proposed as a high-performance anode material for LIBs, SIB, and MIBs.

Herein, we have summarized the key DFT calculation contents and their physicochemical implications discussed in Sections 2 and 3, and systematically compiled them into Table 1 by categorizing based on the intrinsic properties of MXenes and their application characteristics as electrode materials for various rechargeable batteries.

4 Application of machine learning (ML) to MXenes

The tunable surface terminations, versatile X elements (C/N/O), and diverse transition metals collectively endow MXenes with vast theoretical compositional possibilities, giving rise to a large-scale candidate material library. However, traditional trial-and-error experimental approaches and first-principles computational methods are time-consuming, inefficient, and resource-intensive. This makes it challenging to design and evaluate MXene performance for specific application scenarios, thereby constraining the progress of MXene research and even the broader field of materials science. Fortunately, driven by rapid advances in computer science, artificial intelligence (AI), and the Internet of Things (IoT), ML is increasingly recognized as a promising platform to support the development of high-performance MXene electrode materials [2, 116]. By combining efficiency with cost-effectiveness, ML techniques have markedly accelerated research progress in materials discovery, property analysis, performance prediction, and inverse design. Iterative improvements in model accuracy are injecting unprecedented momentum into the development of application-oriented MXene electrodes.

4.1 ML predicts the possibility of MXene material synthesis

Due to the substantial time and cost constraints, the synthesizability of all potential MAX phases cannot be practically evaluated using experimental techniques. Consequently, theoretical calculations are widely employed to efficiently screen unexplored MAX phases, circumventing labor-intensive experimental procedures while providing valuable guidance for subsequent experimental realization. Recent studies have indicated that the thermodynamic stability of compounds can be quantified by the relative formation energy (ΔH) [117, 118]. In the study by Huang *et al.* [119], a ML approach

based on a small dataset was proposed to calculate ΔH for double transition metal MAX phases with the formula $M'_2M''AC_2$ [Fig. 12(a)]. First, a database containing 1320 candidates was constructed by exploring the chemical search space. Subsequently, descriptors derived from elemental information, structural energies, and lattice parameters were generated and selected based on their relative importance. By examining the synergistic effects of key features on ΔH, it was found that both the average electronegativity and the number of unfilled electronic orbitals play a decisive role in determining ΔH. In particular, $M'_2M''AC_2$ candidates with an average electronegativity below 2.24 and more than five unfilled electronic orbitals are more likely to be experimentally synthesized [Figs. 12(b) and (c)]. Additionally, the feasibility of synthesizing 2D $M'_2M''C_2$ was evaluated through a combination of static exfoliation energy, integrated crystal orbital Hamilton population (ICOHP), and phonon spectra calculations, leading to the identification of 75 theoretically accessible candidates. This workflow significantly expedites the screening of MXene properties while reducing the computational cost by more than an order of magnitude.

The stability of materials is considered as a fundamental parameter in nearly all studies, since it strongly affects the cycling performance of batteries. For MXenes, whose layered structures are inherently prone to collapse, structural stability assessments are indispensable before moving forward to experimental validation. He *et al.* [120] employed ML techniques and symbolic regression to evaluate the stability of MXene materials using four different models. The support vector machine algorithm exhibited the highest predictive accuracy in the stability analysis of MXene materials. In addition, symbolic regression has been demonstrated to automatically identify relevant descriptors that govern material stability without relying on prior human-labeled chemical knowledge. Beyond stability prediction, this method provides a rapid and efficient approach for materials classification and the design of novel descriptors, demonstrating broad applicability across diverse materials problems.

4.2 ML predicts the potential of MXenes as electrode materials for energy storage

In rechargeable batteries, the applicability of electrode materials is determined by several essential parameters, among which electrode voltage plays a decisive role. It exerts a direct impact on the energy density, safety, and cycling stability of the device. In the work of Joshi *et al.* [121], the electrode voltage of materials in a metal-ion battery is predicted using deep neural networks, support vector regression, and kernel ridge regression as ML algorithms, in combination with DFT data extracted from the Materials Project database [Fig. 13(a)]. As shown in Fig. 13(b), comparison between the voltage profiles generated by ML methods and those obtained from DFT calculations reveals that the ML models can reliably reproduce the DFT trends, thereby validating their effectiveness in exploring the voltage characteristics of electrode materials. Additionally, this study developed an online tool that enables voltage prediction for any metal-ion battery electrode material within minutes using minimal input information. Another critical performance criterion for electrode materials is the volume change during charging and discharging. In this regard, Moses *et al.* [122] proposed a ML model based on deep neural network regression, quantitatively predicting average voltage and associated volume changes. Model performance was assessed using the mean average absolute error derived from ten-fold cross-validation and an independent test set, confirming its strong predictive accuracy. To further evaluate the screening potential of the constructed model beyond the training database, the authors examined its robustness by applying it to the discovery of novel electrode materials for SIBs. This study identified 22 candidate materials characterized by high energy density and minimal volume change, which were found to exhibit promising electrode properties when benchmarked against DFT+U calculations, showcasing highly encouraging agreement. The correlation between MXene composition and electrochemical performance has also attracted considerable research attention. In this context, Li *et al.* [123] reported the first inverse design of MXene-based battery materials using multi-objective ML, with the workflow illustrated in Fig. 13(c). Within this framework, new categorical descriptors were adopted to classify MXene formulas while predicting multiple target electrochemical properties. Leveraging inverse design, the most suitable MXenes corresponding to specified gravimetric capacity, voltage, and induced charge were identified. Accordingly, the inverse model highlighted Li_2M_2C and Mg_2M_2C (M = Sc, Ti, Cr) as representative candidates meriting in-depth exploration within the specified performance windows.

To enhance the catalytic performance of Li–S battery cathodes, SA modification has emerged as an effective strategy by increasing surface-active sites and optimizing electronic structures. Sun *et al.* [124] screened 11 sulfur-functionalized MXenes (S-MXenes) and identified three materials (Ti_2CS_2, Nb_2CS_2, Ta_2CS_2) that stand out with superior stability and strong LiPSs adsorption, which help suppress the shuttle effect. Building on these three identified S-MXenes, further SA modification with ten transition metals yielded 73 stable SA-S-MXenes. To elucidate how the intrinsic adsorption features of LiPSs affect catalytic behavior, ML was applied to predict the E_{ads} of 1965 possible configurations. The Pearson correlation heatmap [Fig. 13(d)] reveals that the six selected descriptors exhibit low linear correlation coefficients, indicating their independence and suitability for ML

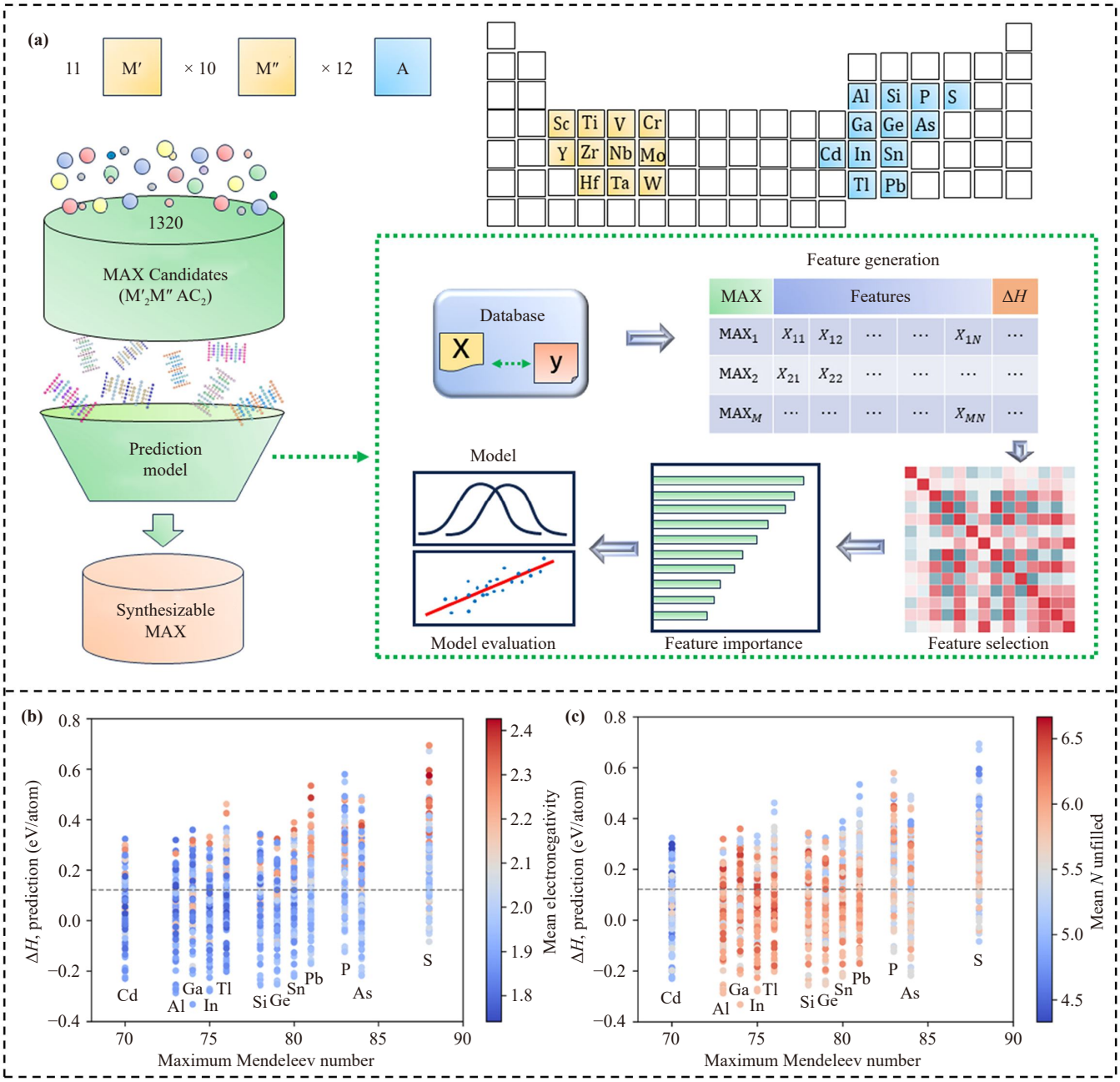

Fig. 12 **(a)** Workflow for predicting synthesizability of $M'_2M''AC_2$ by ML. Correlations of maximum Mendeleev number with **(b)** mean electronegativity and **(c)** with the number of unfilled orbitals in the dataset. Reproduced with permission from Ref. [119]. Copyright © 2025 Elsevier.

modeling. As shown in Fig. 13(e), the trained model achieves high accuracy in predicting E_{ads}, with an R^2 value of 0.88. Feature importance analysis [Fig. 13(f)] indicates that the electronegativity of the SA exerts the greatest influence on E_{ads}. This study not only greatly accelerates the screening of efficient catalysts but also provides valuable guidance for refining LiPSs adsorption models and selecting high-performance catalysts for Li–S batteries.

5 Summary and outlook

From the perspective of theoretical calculations, this review systematically summarizes the progress and future directions of MXene-based electrode materials for rechargeable batteries. DFT calculations, as a powerful approach for understanding material properties and modification mechanisms, have been widely utilized to guide MXene structural design and optimize electrochemical performance. These calculations not only

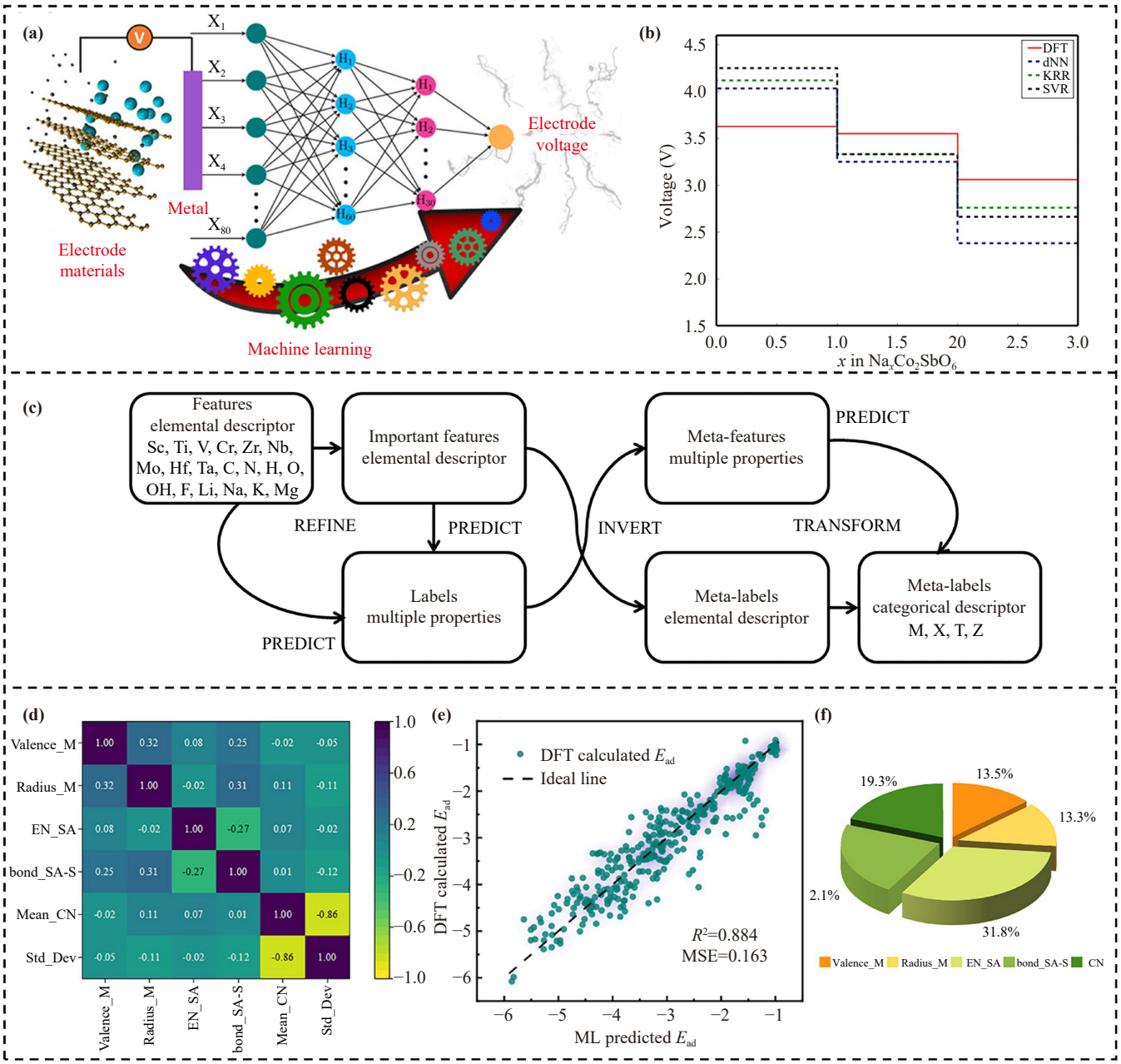

Fig. 13 **(a)** ML-based tool for predicting electrode voltages in metal-ion batteries. **(b)** Comparison of voltage distributions for $Na_xCo_2SbO_6$ predicted by various ML models and DFT. Reproduced with permission from Ref. [121]. Copyright © 2019 American Chemical Society. **(c)** Summary of the workflow showing key steps of model refinement, inversion, and descriptor transformation from regression to classification. Reproduced with permission from Ref. [123]. Copyright © 2022 American Chemical Society. **(d)** Pearson correlation heatmap among selected descriptors. **(e)** Comparison between ML-predicted and DFT-calculated E_{ads} of LiPSs on SA-S-MXenes. **(f)** The pie chart illustrates the feature importance distribution in the XGBoost model. Reproduced with permission from Ref. [124]. Copyright © 2025 John Wiley and Sons.

uncover the intrinsic mechanisms of modification but also provide theoretical support for performance enhancement. When further combined with ML, the construction of efficient descriptors and accurate prediction of structure-property relationships significantly accelerate the design and screening of novel MXene electrodes. This combination offers innovative strategies to overcome existing performance bottlenecks and facilitates broader applications in energy storage technologies.

Despite significant progress in the theoretical investigation of MXene-based electrode materials, several critical challenges remain unresolved. To date, more than 100 MXenes have been predicted through theoretical calculations, whereas only about 40 have been successfully

synthesized experimentally [24], indicating a substantial gap between computational predictions and experimental realization. Future efforts should focus on developing more efficient and controllable synthesis methods while strengthening the integration of theory with experiment. This approach will enable the practical synthesis and application of a broader range of theoretically predicted MXenes. In addition, although current theoretical studies have significantly contributed to our understanding of structural stability, thermodynamic properties, and electrochemical behavior, they are predominantly based on idealized and simplified models that often fail to fully capture the complexity of real experimental conditions. For example, theoretical calculations often assume that MXenes are ideal, defect-free crystalline structures with homogeneously distributed surface terminations, typically focusing on static or near-equilibrium electrochemical reaction environments. These assumptions, however, deviate greatly from realistic experimental conditions. In practical systems, MXenes inevitably contain intrinsic defects, such as vacancies and interlayer distortions, while the types and distributions of surface functional groups are inherently heterogeneous. Moreover, battery operation involves highly complex dynamic processes, including solid–liquid interfacial evolution, interactions between electrolytes and MXene surfaces, and the continuous formation and migration of by-products such as polysulfides or dendrites during charge-discharge cycling [125–127]. Therefore, integrating experimentally relevant factors, including defect structures, electrolyte solvation effects, and dynamic electrochemical processes, into theoretical models, along with establishing quantitative links between computational predictions and experimental observations, remains a key challenge and an important research direction for the development of MXene-based rechargeable batteries. This will lead to more accurate predictions of MXene performance and provide effective guidance for their accelerated deployment in high-performance rechargeable batteries.

In summary, the deep integration of theoretical simulations, artificial intelligence, and advanced characterization techniques is projected to facilitate the rapid discovery and rational screening of novel MXene materials. This progress will be particularly driven under the joint impetus of high-throughput computation and ML. The advancement will not only foster the development of multifunctional electrode materials with high energy density and long cycle stability but will also establish a robust theoretical foundation and design paradigm for the development of next-generation, efficient, safe, and sustainable energy storage systems.

Declarations The authors declare that they have no competing interests and there are no conflicts.

Acknowledgements This work was supported by the Natural Science Foundation of Henan Province (No. 242300421129) and the National Natural Science Foundation of China (No. 52201283).

References

1. J. Zhao, N. Ma, T. Wang, N. Li, Y. Wang, and J. Fan, Theoretical design of high-performance halogen anion batteries with MXene electrodes: Influence of functional groups, metals, and anions, *J. Mater. Chem. A* 10(40), 21611 (2022)
2. S. Sahoo, R. Kumar, I. Hussain, and K. Zhang, Heteroatom doping in 2D MXenes for energy storage/conversion applications, *Adv. Powder Mater.* 3(6), 100246 (2024)
3. J. Aslam, M. A. Waseem, X. M. Lu, S. Wu, W. Sun, and Y. Wang, MXene-infused anode architectures for lithium metal batteries: Pioneering strategies to address core limitations, *Small* 21(32), 2503262 (2025)
4. M. Pandey, K. Deshmukh, A. Raman, A. Asok, S. Appukuttan, and G. R. Suman, Prospects of MXene and graphene for energy storage and conversion, *Renew. Sustain. Energy Rev.* 189, 114030 (2024)
5. P. Xiao, X. Yun, Y. Chen, X. Guo, P. Gao, G. Zhou, and C. Zheng, Insights into the solvation chemistry in liquid electrolytes for lithium-based rechargeable batteries, *Chem. Soc. Rev.* 52(15), 5255 (2023)
6. Z. Rao, P. Lyu, P. Du, D. He, Y. Huo, and C. Liu, Thermal safety and thermal management of batteries, *Battery Energy* 1(3), 20210019 (2022)
7. J. Xie, Q. Chen, H. Zhang, R. Song, and T. Liu, Recent developments of nanocomposite ionogels as monolithic electrolyte membranes for lithium-based batteries, *Battery Energy* 3(1), 20230040 (2024)
8. M. Naguib, M. Kurtoglu, V. Presser, J. Lu, J. Niu, M. Heon, L. Hultman, Y. Gogotsi, and M. W. Barsoum, Two-dimensional nanocrystals produced by exfoliation of Ti_3AlC_2, *Adv. Mater.* 23(37), 4248 (2011)
9. H. Huang and W. Yang, MXene-based micro-supercapacitors: Ink rheology, microelectrode design and integrated system, *ACS Nano* 18(6), 4651 (2024)
10. P. P. Michałowski, M. Anayee, T. S. Mathis, S. Kozdra, A. Wójcik, K. Hantanasirisakul, I. Józwik, A. Piatkowska, M. Mozdzonek, A. Malinowska, R. Diduszko, E. Wierzbicka, and Y. Gogotsi, Oxycarbide MXenes and MAX phases identification using monoatomic layer-by-layer analysis with ultralow-energy secondary-ion mass spectrometry, *Nat. Nanotechnol.* 17(11), 1192 (2022)
11. B. Anasori, M. Naguib, and E. Guest, Two-dimensional MXenes, *MRS Bull.* 48(3), 238 (2023)
12. K. R. G. Lim, M. Shekhirev, B. C. Wyatt, B. Anasori, Y. Gogotsi, and Z. W. Seh, Fundamentals of MXene synthesis, *Nat. Synth.* 1(8), 601 (2022)
13. Y. Wei, P. Zhang, R. A. Soomro, Q. Zhu, and B. Xu, Advances in the synthesis of 2D MXenes, *Adv. Mater.* 33(39), 2103148 (2021)
14. M. A. Hope, A. C. Forse, K. J. Griffith, M. R. Lukatskaya, M. Ghidiu, Y. Gogotsi, and C. P. Grey, NMR reveals the surface functionalisation of Ti_3C_2 MXene, *Phys. Chem. Chem. Phys.* 18(7), 5099 (2016)

15. I. Hussain, W. U. Arifeen, S. A. Khan, S. Aftab, M. S. Javed, S. Hussain, M. Ahmad, X. Chen, J. Zhao, P. Rosaiah, K. F. Fawy, A. Younis, S. Sahoo, and K. Zhang, M_4X_3 MXenes: Application in energy storage devices, *Nano-Micro Lett.* 16(1), 215 (2024)
16. Y. Guan, S. Jiang, Y. Ding, B. Xiao, Y. Pi, Z. Wang, and Y. Cong, Insight into the mechanism of nitrogen doping in MXenes with controllable surface chemistry, *Mater. Today Energy* 44, 101642 (2024)
17. C. Lv, M. Qin, Y. He, M. Wu, and S. Wu, Exploring the potential of 2D Sc_2NX_2 MXene as an anode material for metal-ion (Li^+, Na^+, Mg^{2+}, and Ca^{2+}) batteries: A DFT study, *Comput. Mater. Sci.* 258, 114068 (2025)
18. W. J. Yang, F. L. Liu, Y. X. Lin, J. Wang, C. Zhang, H. Y. Cheng, and H. M. Chen, MXene-based flexible sensors for wearable applications, *Soft Sci.* 5(3), 33 (2025)
19. S. Guan, Y. Liu, S. Liu, Z. Zhuang, R. Shen, H. Zhang, E. Liang, Y. Fan, J. Jiang, B. Liu, Y. Wang, D. Wang, and B. Li, MXene-supported Ru–Ni: A common active site for hydrolysis, hydrogen oxidation, and hydrogenation, *Angew. Chem. Int. Ed.* 64(34), e202506869 (2025)
20. A. Thakur, W. J. Highland, B. C. Wyatt, J. Xu, N. Chandran B. S, B. Zhang, Z. D. Hood, S. P. Adhikari, E. Oveisi, B. Pacakova, F. Vega, J. Simon, C. Fruhling, B. Reigle, M. Asadi, P. P. Michałowski, V. M. Shalaev, A. Boltasseva, T. E. Beechem, C. Liu, and B. Anasori, Synthesis of a 2D tungsten MXene for electrocatalysis, *Nat. Synth.* 4(7), 888 (2025)
21. Z. Shu and Y. Cai, Thickness-dependent catalytic activity of hydrogen evolution based on single atomic catalyst of Pt above MXene, *J. Phys.: Condens. Matter* 35(20), 204001 (2023)
22. W. Yan, A. Rafieerad, K. N. Alagarsamy, L. R. Saleth, R. C. Arora, and S. Dhingra, Immunoengineered MXene nanosystem for mitigation of alloantigen presentation and prevention of transplant vasculopathy, *Nano Today* 48, 101706 (2023)
23. K. N. Alagarsamy, L. R. Saleth, S. Sekaran, L. Fusco, L. G. Delogu, M. Pogorielov, A. Yilmazer, and S. Dhingra, MXenes as emerging materials to repair electroactive tissues and organs, *Bioact. Mater.* 48, 583 (2025)
24. Y. Jiang, J. Lao, G. Dai, and Z. Ye, Advanced insights on MXenes: Categories, properties, synthesis, and applications in alkali metal ion batteries, *ACS Nano* 18(22), 14050 (2024)
25. Y. Ji, X. Zhang, W. Ai, Z. He, S. Lou, Z. Tang, F. Hang, Z. Liu, Y. Ou, X. Hu, and P. Zong, Intercalation-deintercalation engineering of van der Waals stacked MXene films for wearable thermoelectrics and sensing, *Chem. Eng. J.* 512, 162603 (2025)
26. J. Li, S. Xi, T. Lei, R. Yao, F. Zeng, J. Wu, S. Tu, and X. Liu, Machine learning assisted prediction in the discharge capacities of novel MXene cathodes for aluminum ion batteries, *J. Energy Storage* 82(30), 110196 (2024)
27. Y. Qin, W. Zhao, T. Wang, W. Liu, T. Zhou, X. Han, Y. Liu, J. Hu, and Q. Jiang, Construction of waffle-like NS-ZIF@V_2CT_x heterostructures for high-performance potassium-ion batteries, *J. Mater. Chem. A* 13(30), 24633 (2025)
28. Y. Liu, K. Guo, Y. Ge, W. Yan, K. Gu, Y. Tian, and X. Cui, Structural engineering of MXenes towards high electrochemical performance in supercapacitors, *Int. J. Miner. Metall. Mater.* 32(8), 1783 (2025)
29. Z. Huang, M. Farahmandjou, F. Marlton, X. Guo, H. Gao, B. Sun, and G. Wang, Surface and structure engineering of MXenes for rechargeable batteries beyond lithium, *J. Materiomics* 10(1), 253 (2024)
30. R. Wang, M. Li, Y. Zhang, K. Sun, and W. Bao, Atomic surface modification strategy of MXene materials for high-performance metal sulfur batteries, *Int. J. Energy Res.* 46(9), 11659 (2022)
31. J. Shi, M. Du, Y. Chen, Q. Li, D. Xu, G. Zhang, and H. Pang, MXene functionalized cathodes, anodes, and separators for batteries, *Chem. Eng. J.* 507, 160809 (2025)
32. Q. Guan, H. Yan, and Y. Cai, Strongly modulated exfoliation and functionalization of MXenes with rationally designed groups in polymer: A theoretical study, *Chem. Mater.* 34(21), 9414 (2022)
33. P. Ma, D. Fang, Y. Liu, Y. Shang, Y. Shi, and H. Y. Yang, MXene-based materials for electrochemical sodium-ion storage, *Adv. Sci. (Weinh.)* 8(11), 2003185 (2021)
34. I. A. Soomro, M. N. Lakhan, A. Hanan, H. Almujibah, A. Hussain, A. H. Pato, M. Ahmed, I. A. Chandio, S. A. Memon, M. Umer, F. Bibi, and M. Lei, 2D MXenes as electrode materials for metal-sulfur batteries: A review, *Mater. Today Phys.* 45, 101453 (2024)
35. S. He, X. Sun, H. Zhang, C. Yuan, Y. Wei, and J. Li, Preparation strategies and applications of MXene-polymer composites: A review, *Macromol. Rapid Commun.* 42(19), 2100324 (2021)
36. J. Gao, J. Li, Q. Wang, and C. Zou, Progress of MXene-based materials in the field of rechargeable batteries, *Materials (Basel)* 18(10), 2386 (2025)
37. J. Sun, R. Yu, D. Legut, J. S. Francisco, and R. Zhang, Rational design of highly stable and active single-atom modified S-MXene as cathode catalysts for Li–S batteries, *Adv. Mater.* 37(28), 2501523 (2025)
38. C. Zheng, Y. Yao, X. Rui, Y. Feng, D. Yang, H. Pan, and Y. Yu, Functional MXene-based materials for next-generation rechargeable batteries, *Adv. Mater.* 34(51), 2204988 (2022)
39. Z. You, D. Lu, K. K. Kondamareddy, W. Gu, P. Cheng, J. Yang, R. Zheng, and H. Wang, Preparation and modification of MXene composites for application in electrochemical energy storage, *J. Electrochem.* 31(5), 2418001 (2025)
40. Z. Liu, Y. Tian, J. Yang, S. Xu, Q. Tian, P. Yan, B. Han, and Q. Xu, Ultrafast ion transport in 2D confined MXene for improved electrochemical performance: Boron-atom-substituted –OH termination, *ACS Nano* 18(47), 32950 (2024)
41. V. Kamysbayev, A. S. Filatov, H. Hu, X. Rui, F. Lagunas, D. Wang, R. F. Klie, and D. V. Talapin, Covalent surface modifications and superconductivity of two-dimensional metal carbide MXenes, *Science* 369(6506), 979 (2020)

42. S. Kajiyama, L. Szabova, K. Sodeyama, H. Iinuma, R. Morita, K. Gotoh, Y. Tateyama, M. Okubo, and A. Yamada, Sodium-ion intercalation mechanism in MXene nanosheets, *ACS Nano* 10(3), 3334 (2016)
43. Y. Luo, W. Que, Y. Tang, Y. Kang, X. Bin, Z. Wu, B. Yuliarto, B. Gao, J. Henzie, and Y. Yamauchi, Regulating functional groups enhances the performance of flexible microporous MXene/bacterial cellulose electrodes in supercapacitors, *ACS Nano* 18(18), 11675 (2024)
44. J. Pang, R. G. Mendes, A. Bachmatiuk, L. Zhao, H. Q. Ta, T. Gemming, H. Liu, Z. Liu, and M. H. Rummeli, Applications of 2D MXenes in energy conversion and storage systems, *Chem. Soc. Rev.* 48(1), 72 (2019)
45. Q. Tang, Z. Zhou, and P. Shen, Are MXenes promising anode materials for Li ion batteries? Computational studies on electronic properties and li storage capability of Ti_3C_2 and $Ti_3C_2X_2$ (X = F, OH) monolayer, *J. Am. Chem. Soc.* 134(40), 16909 (2012)
46. Y. Xie, M. Naguib, V. N. Mochalin, M. W. Barsoum, Y. Gogotsi, X. Yu, K. Nam, X. Yang, A. I. Kolesnikov, and P. R. C. Kent, Role of surface structure on Li-ion energy storage capacity of two-dimensional transition-metal carbides, *J. Am. Chem. Soc.* 136(17), 6385 (2014)
47. J. Wang, L. Hao, J. Qin, X. Zhang, Y. Cheng, L. Yue, Y. Wang, M. Jiang, Z. Wang, and M. Cao, Iodine-redox-chemistry-modulated ion transport channels in MXene enables high energy storage capacity, *Energy Storage Mater.* 66, 103209 (2024)
48. X. Chen, Y. Zhu, M. Zhang, J. Sui, W. Peng, Y. Li, G. Zhang, F. Zhang, and X. Fan, N-butyllithium-treated $Ti_3C_2T_x$ MXene with excellent pseudocapacitor performance, *ACS Nano* 13(8), 9449 (2019)
49. T. Bashir, S. A. Ismail, J. Wang, W. Zhu, J. Zhao, and L. Gao, MXene terminating groups =O, –F or –OH, –F or =O, –OH, –F, or =O, –OH, –Cl, *J. Energy Chem.* 76, 90 (2023)
50. N. Zhang, Y. Hong, S. Yazdanparast, and M. Asle Zaeem, Superior structural, elastic and electronic properties of 2D titanium nitride MXenes over carbide MXenes: A comprehensive first principles study, *2D Mater.* 5(4), 045004 (2018)
51. M. P. Bilibana, Electrochemical properties of MXenes and applications, *Adv. Sens. Energy Mater.* 2(4), 100080 (2023)
52. D. Li, X. Chen, P. Xiang, H. Du, and B. Xiao, Chalcogenated-$Ti_3C_2X_2$ MXene (X = O, S, Se and Te) as a high-performance anode material for Li-ion batteries, *Appl. Surf. Sci.* 501, 144221 (2020)
53. Y. Yang, M. Han, C. E. Shuck, R. K. Sah, J. R. Paudel, A. X. Gray, Y. Gogotsi, and S. J. May, Correlating electronic properties with M-site composition in solid solution $Ti_yNb_{2-y}CT_x$ MXenes, *2D Mater.* 10(1), 14011 (2022)
54. J. Zhao, W. Yan, Z. Liu, X. Liu, Y. Tian, and X. Cui, Optimizing electronic structure of $Mo_2TiC_2T_x$ MXene through Nb doping for enhanced electrochemical performance, *Nano Res.* 17(8), 7174 (2024)
55. Z. Shu, Z. Shi, M. F. Ng, T. L. Tan, and Y. Cai, Unveiling the effect of solvent for hydrogen evolution in Pt-doped MXenes and corresponding high-entropy phase, *Mater. Today Sustain.* 26, 100808 (2024)
56. M. Khazaei, M. Arai, T. Sasaki, C. Y. Chung, N. S. Venkataramanan, M. Estili, Y. Sakka, and Y. Kawazoe, Novel electronic and magnetic properties of two-dimensional transition metal carbides and nitrides, *Adv. Funct. Mater.* 23(17), 2185 (2013)
57. D. A. Kuznetsov, Z. X. Chen, P. V. Kumar, A. Tsoukalou, A. Kierzkowska, P. M. Abdala, O. V. Safonova, A. Fedorov, and C. R. Müller, Single site cobalt substitution in 2D molybdenum carbide (MXene) enhances catalytic activity in the hydrogen evolution reaction, *J. Am. Chem. Soc.* 141(44), 17809 (2019)
58. K. Li, J. Zeng, Y. Wang, J. Zhang, and Y. Zhou, A first-principles study of the lithium storage properties of transition metal doped TM-Ti_2CO_2 (TM=Sc, V, Cr, Mn, Fe, Co, Ni and Cu), *Mater. Today Commun.* 40, 109718 (2024)
59. Z. Du, C. Wu, Y. Chen, Z. Cao, R. Hu, Y. Zhang, J. Gu, Y. Cui, H. Chen, Y. Shi, J. Shang, B. Li, and S. Yang, High-entropy atomic layers of transition-metal carbides (MXenes), *Adv. Mater.* 33(39), 2101473 (2021)
60. A. Dey, S. Varagnolo, N. P. Power, N. Vangapally, Y. Elias, L. Damptey, B. N. Jaato, S. Gopalan, Z. Golrokhi, P. Sonar, V. Selvaraj, D. Aurbach, and S. Krishnamurthy, Doped MXenes - a new paradigm in 2D systems: Synthesis, properties and applications, *Prog. Mater. Sci.* 139, 101166 (2023)
61. W. Zhang, S. Liu, J. Chen, F. Hu, X. Wang, H. Huang, and M. Yao, Exploring the potentials of $Ti_3C_iN_{2-i}T_x$ (i = 0, 1, 2)-MXene for anode materials of high-performance sodium-ion batteries, *ACS Appl. Mater. Interfaces* 13(19), 22341 (2021)
62. C. Lu, L. Yang, B. Yan, L. Sun, P. Zhang, W. Zhang, and Z. Sun, Nitrogen-doped Ti_3C_2 MXene: Mechanism investigation and electrochemical analysis, *Adv. Funct. Mater.* 30(47), 2000852 (2020)
63. K. Hantanasirisakul, M. Alhabeb, A. Lipatov, K. Maleski, B. Anasori, P. Salles, C. Ieosakulrat, P. Pakawatpanurut, A. Sinitskii, S. J. May, and Y. Gogotsi, Effects of synthesis and processing on optoelectronic properties of titanium carbonitride MXene, *Chem. Mater.* 31(8), 2941 (2019)
64. W. Cui, S. Chen, J. Duan, and R. Zhang, Surface functional group regulation of $Ti_3C_2T_x$ based on atmospheric pressure cold plasma, *Contrib. Plasma Phys.* 64(9), e202300103 (2024)
65. B. Ahmed, M. B. Tahir, A. Ali, and M. Sagir, Exploring the structural and electronic properties of N-doped Ti_2C MXenes for novel applications in advanced materials and devices: A DFT study, *Mater. Sci. Semicond. Process.* 186, 109091 (2025)
66. N. Wu, J. Shen, X. Zhou, S. Li, J. Li, G. Liu, D. Guo, W. Deng, C. Yuan, X. Liu, and H. Hou, Constructing iron vacancies in thiospinel $FeIn_2S_4$ to modulate Fe d-band center and accelerate sodiation kinetics enabling high-rate and durable sodium storage, *Adv. Energy Mater.* 15(19), 2405729 (2025)
67. T. Hu, J. Yang, and X. Wang, Carbon vacancies in Ti_2CT_2 MXenes: Defects or a new opportunity, *Phys.*

Chem. Chem. Phys. 19(47), 31773 (2017)
68. H. Wu, Z. Guo, J. Zhou, and Z. Sun, Vacancy-mediated lithium adsorption and diffusion on MXene, *Appl. Surf. Sci.* 488, 578 (2019)
69. S. Li, K. Guan, D. Zhou, D. Zou, J. Lu, W. Jiang, B. Chen, J. Qiu, L. Cui, T. Yu, Y. Sun, Z. Xu, W. Jin, and W. Jing, Lattice vacancy-anchored perforation of 2D MXenes for crafting nanochannel membranes with spontaneous multi-level features, *ACS Nano* 19(5), 5178 (2025)
70. R. Ibragimova, P. Rinke, and H. P. Komsa, Native vacancy defects in MXenes at etching conditions, *Chem. Mater.* 34(7), 2896 (2022)
71. M. R. Lukatskaya, O. Mashtalir, C. E. Ren, Y. Dall' Agnese, P. Rozier, P. L. Taberna, M. Naguib, P. Simon, M. W. Barsoum, and Y. Gogotsi, Cation intercalation and high volumetric capacitance of two-dimensional titanium carbide, *Science* 341(6153), 1502 (2013)
72. J. Li, M. Lu, W. Zheng, and W. Zhang, Ion-intercalation architecture for robust functionalization of two-dimensional MXenes, *Energy Storage Mater.* 64, 103068 (2024)
73. K. Subramanyan, S. Chen, N. Li, T. Ma, Y. Liu, S. Chandrasekaran, and V. Aravindan, Multi-layered MXene $V_4C_3T_x$ as new low-voltage insertion anode for Na-ion battery applications, *Electrochim. Acta* 437, 141505 (2023)
74. X. Yin, W. Zheng, H. Tang, L. Yang, C. Lu, L. Pan, P. Zhang, and Z. Sun, Unraveling cation intercalation mechanism in MXene for enhanced supercapacitor performance, *Energy Storage Mater.* 72, 103688 (2024)
75. K. Arole, S. E. Pas, R. M. Thakur, L. A. Amiouny, M. H. Kabir, M. Dujovic, M. Radovic, J. L. Lutkenhaus, M. J. Green, and H. Liang, Effects of intercalation on ML-$Ti_3C_2T_z$ MXene properties and friction performance, *ACS Appl. Mater. Interfaces* 16(46), 64156 (2024)
76. C. Wei, T. Fang, X. Tang, K. Jiang, and X. Liu, Ti_2CT_2 MXene as anodes for metal ion batteries: From monolayer to bilayer to pillar structure, *Langmuir* 38(38), 11732 (2022)
77. Y. T. Du, X. Kan, F. Yang, L. Y. Gan, and U. Schwingenschlögl, MXene/graphene heterostructures as high-performance electrodes for Li-ion batteries, *ACS Appl. Mater. Interfaces* 10(38), 32867 (2018)
78. Q. Kong, X. An, L. Huang, X. Wang, W. Feng, S. Qiu, Q. Wang, and C. Sun, A DFT study of $Ti_3C_2O_2$ MXenes quantum dots supported on single layer graphene: Electronic structure an hydrogen evolution performance, *Front. Phys. (Beijing)* 16(5), 53506 (2021)
79. S. R. K. A, N. Barman, S. Radhakrishnan, R. Thapa, and C. S. Rout, Hierarchical architecture of the metallic $VTe_2/Ti_3C_2T_x$ MXene heterostructure for supercapacitor applications, *J. Mater. Chem. A* 10(44), 23590 (2022)
80. Q. Guan, H. Yan, and Y. Cai, Flatten the Li-ion activation in perfectly lattice-matched MXene and 1T-MoS_2 heterostructures via chemical functionalization, *Adv. Mater. Interfaces* 9(7), 2101838 (2022)
81. W. Xi, J. Jin, Y. Zhang, R. Wang, Y. Gong, B. He, and H. Wang, Hierarchical MXene/transition metal oxide heterostructures for rechargeable batteries, capacitors, and capacitive deionization, *Nanoscale* 14(33), 11923 (2022)
82. Y. Aierken, C. Sevik, O. Gülseren, F. M. Peeters, and D. Çakır, MXenes/graphene heterostructures for Li battery applications: A first principles study, *J. Mater. Chem. A* 6(5), 2337 (2018)
83. T. Wang, J. Zhao, L. Qi, G. Li, W. Yang, and Y. Li, Ultrathin graphdiyne oxide-intercalated MXene: A new heterostructure with interfacial synergistic effect for high performance lithium-ion storage, *Energy Storage Mater.* 54, 10 (2023)
84. W. Ji, Y. Peng, Y. Wang, S. Zhao, and N. Zhou, Enhancing MXene-based anodes with two-dimensional VO_2/V_2CO_2 heterostructures: A first-principles calculations study, *Comput. Mater. Sci.* 249, 113615 (2025)
85. M. R. Palacín and A. de Guibert, Why do batteries fail, *Science* 351(6273), 1253292 (2016)
86. J. Xu, Y. Dou, Z. Wei, J. Ma, Y. Deng, Y. Li, H. Liu, and S. Dou, Recent progress in graphite intercalation compounds for rechargeable metal (Li, Na, K, Al)-ion batteries, *Adv. Sci. (Weinh.)* 4(10), 1700146 (2017)
87. C. Wang, I. Kakwan, A. J. Appleby, and F. E. Little, In situ investigation of electrochemical lithium intercalation into graphite powder, *J. Electroanal. Chem.* 489(1–2), 55 (2000)
88. C. Eames and M. S. Islam, Ion intercalation into two-dimensional transition-metal carbides: Global screening for new high-capacity battery materials, *J. Am. Chem. Soc.* 136(46), 16270 (2014)
89. X. Zhao, P. Wang, E. Lv, C. Wu, K. Ma, Z. Gao, I. D. Gates, and W. Yang, Screening MXenes for novel anode material of lithium-ion batteries with high capacity and stability: A DFT calculation, *Appl. Surf. Sci.* 569, 151050 (2021)
90. H. Wang, W. Jiang, X. Ma, R. Ma, X. Zhang, Y. Fang, M. Jiao, and Z. Zhou, Screening functionalized Ti_3C_2 MXenes as promising anode candidates for alkali metal ion batteries, *Chem. Commun. (Camb.)* 61(90), 17621 (2025)
91. M. Wei, H. Wang, J. Zhu, Y. Liu, Y. Fu, Q. Hu, and A. Zhou, Performance of –S and –O bifunctional V_2C MXene monolayer in lithium-ion batteries: A first-principles study, *J. Energy Storage* 102, 114255 (2024)
92. M. Zhou, Y. Shen, L. Lv, Y. Zhang, X. Meng, X. Yang, Q. He, B. Zhang, and Z. Zhou, Bare W-based MXenes (WCrC and MoWC) anode with high specific capacity for Li and Mg-ion batteries, *J. Phys. D* 57(1), 015502 (2024)
93. P. Chen, N. Li, X. Chen, W. J. Ong, and X. Zhao, The rising star of 2D black phosphorus beyond graphene: Synthesis, properties and electronic applications, *2D Mater.* 5(1), 014002 (2018)
94. S. Saharan, U. Ghanekar, and S. Meena, Black phosphorus/V_3C_2 MXene layered heterostructure as a sustainable cathode material for Li-ion battery: An ab initio study, *J. Phys. Chem. C* 127(19), 8905 (2023)
95. S. S. Zhang, Liquid electrolyte lithium/sulfur battery: Fundamental chemistry, problems, and solutions, *J. Power Sources* 231, 153 (2013)

96. T. Ma, H. Yue, Y. Xiao, Y. Huang, X. Li, X. Gao, N. He, C. Zhan, and D. Nan, A review of organic sulfur applications in lithium–sulfur batteries, *J. Power Sources* 625, 235717 (2025)
97. D. Rao, L. Zhang, Y. Wang, Z. Meng, X. Qian, J. Liu, X. Shen, G. Qiao, and R. Lu, Mechanism on the improved performance of lithium sulfur batteries with MXene-based additives, *J. Phys. Chem. C* 121(21), 11047 (2017)
98. D. Wang, F. Li, R. Lian, J. Xu, D. Kan, Y. Liu, G. Chen, Y. Gogotsi, and Y. Wei, A general atomic surface modification strategy for improving anchoring and electrocatalysis behavior of $Ti_3C_2T_2$ MXene in lithium–sulfur batteries, *ACS Nano* 13(10), 11078 (2019)
99. M. Xu, Q. Zhu, Y. Li, Y. Gao, N. Sun, and B. Xu, Atom-dominated relay catalysis of high-entropy MXene promotes cascade polysulfide conversion for lithium–sulfur batteries, *Energy Environ. Sci.* 17(20), 7735 (2024)
100. M. Ge, C. Wei, X. Tang, T. Fang, and X. Liu, Heterostructures of mxene and graphene as cathode hosts improving anchoring and reaction dynamics for Li–S batteries, *Ind. Eng. Chem. Res.* 63(38), 16399 (2024)
101. G. Zhou, S. Zhao, T. Wang, S. Z. Yang, B. Johannessen, H. Chen, C. Liu, Y. Ye, Y. Wu, Y. Peng, C. Liu, S. P. Jiang, Q. Zhang, and Y. Cui, Theoretical calculation guided design of single-atom catalysts toward fast kinetic and long-life Li–S batteries, *Nano Lett.* 20(2), 1252 (2020)
102. X. Chi, M. Li, J. Di, P. Bai, L. Song, X. Wang, F. Li, S. Liang, J. Xu, and J. Yu, A highly stable and flexible zeolite electrolyte solid-state Li–air battery, *Nature* 592(7855), 551 (2021)
103. C. Wei, Z. Shi, M. Tian, M. Chao, A. Zhou, J. Sun, Y. Song, J. Li, and R. Yang, Synergistic engineering on surface chemistry and morphology in $Ti_3C_2T_x$ MXene towards high rate and durable LiO_2 batteries, *J. Colloid Interface Sci.* 702, 138845 (2026)
104. D. Zhao, P. Wang, H. Di, P. Zhang, X. Hui, and L. Yin, Single semi-metallic selenium atoms on Ti_3C_2 MXene nanosheets as excellent cathode for lithium–oxygen batteries, *Adv. Funct. Mater.* 31(29), 2010544 (2021)
105. R. Ren, Y. Fu, M. Huang, Z. Li, Y. Lu, and Q. Liu, Three-atom bridged centers activate inert electrons in MXene via Ti 3d orbital engineering to enhance electrocatalysis in lithium–oxygen batteries, *Chem. Eng. J.* 519, 165538 (2025)
106. P. Liu, H. Xu, X. Wang, G. Tian, X. Wen, C. Wang, C. Zeng, S. Wang, F. Fan, T. Zeng, S. Liu, and C. Shu, Bimetallic MXene with tailored vanadium d-band as highly efficient electrocatalyst for reversible lithium-oxygen battery, *J. Colloid Interface Sci.* 655, 364 (2024)
107. Y. Dong, J. Huo, C. Xu, D. Ji, H. Zhao, L. Li, and Y. Lei, Research progress on vanadium sulfide anode materials for sodium and potassium-ion batteries, *Adv. Mater. Technol.* 9(11), 2301840 (2024)
108. T. Hosaka, K. Kubota, A. S. Hameed, and S. Komaba, Research development on K-ion batteries, *Chem. Rev.* 120(14), 6358 (2020)
109. A. K. X. Tan and S. Paul, Beyond lithium: Future battery technologies for sustainable energy storage, *Energies* 17(22), 5768 (2024)
110. X. Li, M. Li, Q. Yang, G. Liang, Z. Huang, L. Ma, D. Wang, F. Mo, B. Dong, Q. Huang, and C. Zhi, In situ electrochemical synthesis of MXenes without acid/alkali usage in/for an aqueous zinc ion battery, *Adv. Energy Mater.* 10(36), 2001791 (2020)
111. M. K. Masood, J. Wang, J. Song, and Y. Liu, A novel two-dimensional monolayer MB_4 (M = Cr, Mo, W) MBenes as a high-performance anode material for Mg-ion batteries, *J. Energy Storage* 86, 111370 (2024)
112. J. Guo, D. Hu, C. Bai, L. Xu, H. Xiao, Q. Shi, X. Li, X. Chen, Y. Ma, and G. Fang, Structural and electrochemical properties of $Ta_{n+1}C_n$ MXene anode materials for metal-ion batteries, *Inorg. Chem. Front.* 11(10), 2945 (2024)
113. T. Bai, H. Liu, B. Chen, Y. Qiu, H. Dong, K. Wu, Y. Cheng, and B. Xiao, Assessing $(Mo_{2/3}Sc_{1/3})_2C$ and $(Mo_{2/3}Sc_{1/3})_2CT_2$ (T = –O, –OH, and –F) i-MXenes as high-performance electrode materials for lithium and non-lithium ion batteries, *J. Phys. Chem. C* 126(25), 10273 (2022)
114. M. Qin, C. Lv, Y. He, S. Wu, M. Wu, Q. Zhu, and M. Kuang, Zr_2CSSe Janus MXene as electrode materials for metal (Na, K, Mg, Ca) ion batteries: A DFT study, *Surf. Interfaces* 72, 107397 (2025)
115. F. Ma, X. Zhao, H. Luo, C. Shang, H. Gao, and X. Wang, Insights into $Ti_3N_2T_2/VS_2$ (T = F, O, OH) heterostructures as innovative anode materials for lithium/sodium/magnesium-ion batteries, *J. Mater. Chem. A* 12(34), 23008 (2024)
116. C. Deng, X. Ji, C. Rainey, J. Zhang, and W. Lu, Integrating machine learning with human knowledge, *iScience* 23(11), 101656 (2020)
117. G. R. Schleder, C. M. Acosta, and A. Fazzio, Exploring two-dimensional materials thermodynamic stability via machine learning, *ACS Appl. Mater. Interfaces* 12(18), 20149 (2020)
118. C. J. Bartel, A. W. Weimer, S. Lany, C. B. Musgrave, and A. M. Holder, The role of decomposition reactions in assessing first-principles predictions of solid stability, *npj Comput. Mater.* 5(1), 4 (2019)
119. Z. Huang, Y. Li, F. Wei, Y. Wang, M. Zhang, R. Ma, and W. Zhao, Prediction of synthesis of ternary-layered double transition metal MAX phases and the possibility of their exfoliation for formation of 2D MXenes, *Surf. Interfaces* 56, 105518 (2025)
120. M. He and L. Zhang, Machine learning and symbolic regression investigation on stability of MXene materials, *Comput. Mater. Sci.* 196, 110578 (2021)
121. R. P. Joshi, J. Eickholt, L. Li, M. Fornari, V. Barone, and J. E. Peralta, Machine learning the voltage of electrode materials in metal-ion batteries, *ACS Appl. Mater. Interfaces* 11(20), 18494 (2019)
122. I. A. Moses, R. P. Joshi, B. Ozdemir, N. Kumar, J. Eickholt, and V. Barone, Machine learning screening of metal-ion battery electrode materials, *ACS Appl. Mater. Interfaces* 13(45), 53355 (2021)

123. S. Li and A. S. Barnard, Inverse design of MXenes for high-capacity energy storage materials using multi-target machine learning, *Chem. Mater.* 34(11), 4964 (2022)
124. J. Sun, R. Yu, D. Legut, J. S. Francisco, and R. Zhang, Rational design of highly stable and active single-atom modified S-MXene as cathode catalysts for Li–S batteries, *Adv. Mater.* 37(28), 2501523 (2025)
125. M. Tian, Z. Wang, H. Y. Yang, and S. Chen, Recent progress in computational materials science boosting development of rechargeable batteries, *Adv. Energy Mater.* 15(1), 2403443 (2025)
126. S. Zhang, J. Ma, S. Dong, and G. Cui, Designing all-solid-state batteries by theoretical computation: A review, *Electrochem. Energy Rev.* 6(1), 4 (2023)
127. L. Xia, H. Liu, and Y. Pei, Theoretical calculations and simulations power the design of inorganic solid-state electrolytes, *Nanoscale* 16(33), 15481 (2024)